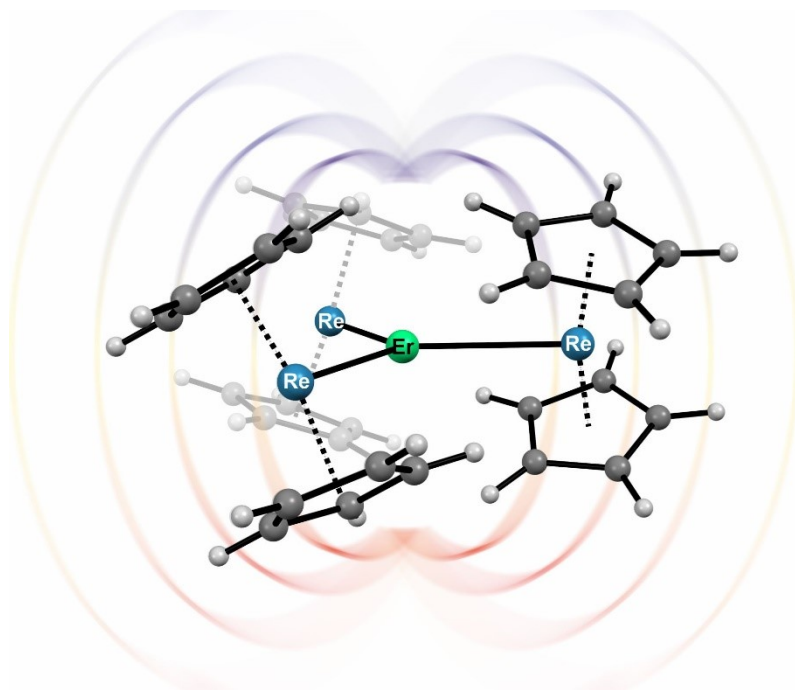


An 'Intermetallic' Molecular Nanomagnet with the Lanthanide Coordinated Only by Transition Metals



Michał Magott,¹ Maria Brzozowska,¹ Stanisław Baran,² Veacheslav Vieru,³ Dawid Pinkowicz^{1,}*

¹ Faculty of Chemistry, Jagiellonian University, Gronostajowa 2, 30-387 Kraków, Poland

² Marian Smoluchowski Institute of Physics, Jagiellonian University, Łojasiewicza 11, 30-348 Kraków, Poland

³ Maastricht Science Programme, Faculty of Science and Engineering, Maastricht University, Paul-Henri Spaaklaan 1, 6229 EN Maastricht, The Netherlands

*Correspondence: dawid.pinkowicz@uj.edu.pl

Keywords

Lanthanide complexes, lanthanide-transition metal bonds, organometallic chemistry, molecular magnetism, single molecule magnet, molecular nanomagnet, magnetic memory

Summary

The best performing molecular nanomagnets are currently designed by carefully arranging *p*-element donor atoms (usually carbon, nitrogen and/or oxygen) around the central magnetic ion. Inspired by the structure of the hardest intermetallic magnet SmCo₅, we have demonstrated a nanomagnetic molecule where the central lanthanide (Ln) ion Er^{III} is coordinated solely by three transition metal (TM) ions in a perfectly trigonal planar fashion. The molecule [Er^{III}(Re^ICp₂)₃] (**ErRe₃**) constitutes the first example of a molecular nanomagnet (MNM; or single molecule magnet SMM) with unsupported Ln-TM bonds and paves the way towards molecular intermetallics with strong direct magnetic exchange interactions. Such interactions are believed to be crucial for quenching the quantum tunneling of magnetization which limits the application of Ln-SMMs as sub-nanometer magnetic memory units.

Introduction

Rare-earth intermetallic magnets – samarium-cobalt (SmCo)¹ and neodymium (NdFeB)^{2,3} – are the strongest permanent magnets known to date with multiple applications in modern technology ranging from hard disk drives to electric vehicles and wind turbines.⁴ Their commercial success results from the combination of the strong magnetic anisotropy of rare earths and their direct magnetic coupling with transition metal ions. At the other far end of the current search for novel magnetic materials are magnetic molecules, called molecular nanomagnets⁵ (MNMs) or single molecule magnets (SMMs). MNMs are molecule-sized objects with magnetic memory effects governed by quantum mechanics.⁶⁻¹⁰ They are strongly believed to revolutionize magnetic information storage, but at the moment do not have any real-world applications, as their performance is limited by low blocking temperatures and quantum tunneling of magnetization (QTM).¹¹ Current trends in the design of MNMs^{12,13} were ignited by the discovery of terbium double-decker [TbPc₂]⁻ (Pc = phthalocyanine dianion)¹⁴ and were fueled by the seminal perspective of Rinehart and Long.¹⁵ Design principles focus on the precise control of the coordination sphere of a single lanthanide center in order to maximize the easy-axis magnetic anisotropy of the complex and to limit the spin-lattice relaxation rates.¹⁶⁻¹⁹ While this approach led to several breakthroughs, including the observation of the magnetic hysteresis loop of molecular origin above the liquid nitrogen barrier for dysprosocenium^{6,7} and magnetic field control of the magnetization blocking barrier,²⁰ it appears to be reaching its limit as the proposed modifications were not as successful as expected.^{21,22}

The original approach to MNMs was based on designing multinuclear systems with strong magnetic superexchange, where several paramagnetic centers are "glued" together by bridging ligands to form a high-spin molecule. If magnetic anisotropy is present in such a system, it shows MNM properties.^{23,24} An MNM of this type stands behind the success story of the whole field as it was indeed started by the discovery of a dodecanuclear carboxylate-bridged cluster Mn₁₂ – a high-spin molecule (*S* = 10) comprising eight Mn^{III} and four Mn^{IV} ions interacting magnetically via the bridging carboxylate ligands.²⁵⁻²⁷ However, the indirect character of these magnetic interactions, based on weak superexchange coupling mechanism, limits the performance of Mn₁₂ to very low temperatures, below the boiling point of liquid helium.

Attempts to adapt this particular strategy to dysprosocenium complexes suffer from a similar problem – weak superexchange interactions of the lanthanides with other metal centers through diamagnetic bridging ligands limit their influence on the slow magnetic relaxation.²⁸⁻³⁰ Therefore, the route towards the high-performance MNMs based on superexchange interactions has been largely abandoned.

Overall, despite the huge progress in the field initiated by Mn₁₂, its ultimate goal – the room-temperature molecular nanomagnet (RT-MNM) – remains elusive. However, the aforementioned examples of the rare-earth intermetallics: SmCo₅¹ and Nd₂Fe₁₄B² provide clues for the possible direction in the design of RT-MNMs. Focusing the efforts on molecules comprising a rare-earth metal center coordinated solely by transition metal ions,³¹⁻³⁴ mimicking the first coordination sphere of the Sm center in the SmCo₅ magnet (Figure 1A-1C) could enable the appearance of the direct exchange coupling between the highly anisotropic lanthanide central ion and the coordinated transition metals. This approach was recently predicted to efficiently suppress QTM in MNMs³⁵ and demonstrated for the ultra-hard MNM (Cp₂Pr₅)₂Dy₂I₃ where direct *f-f* exchange is operational.³⁶ Interestingly, even much weaker indirect interactions were reported to be quite efficient in this matter.³⁷

The concept of unsupported bonds between the lanthanide and the transition metal was first introduced and explored by Kempe et al.^{32, 34} Later, it was proposed by Rinehart and Long¹⁵ as a possible strategy towards molecular nanomagnets and put to use by Nippe et al. reporting MNMs with unsupported direct bonds between the dysprosium ion and 4*d* (Fe) or 4*d* (Ru) transition metal ions.³⁸ However, the magnetic memory effect (magnetic hysteresis) has not been observed, most probably due to the unfavorable ligand field geometry³⁸ or the unfortunate choice of the rare-earth metal.³² Noteworthy, the introduction of *p*-block heavy metals directly into the coordination sphere of the lanthanide was also pursued resulting in interesting examples of MNMs.^{39, 40}

Here, we apply the principles of easy-axis magnetic anisotropy design with the methodology of Kempe et al. that led previously to rare-earth metal complexes coordinated solely by transition metals.³² Herein, we demonstrate the first step toward molecular "intermetallic" nanomagnets, a perfectly trigonal planar [Er^{III}(Re^ICp₂)₃] complex (**ErRe₃**; Cp = cyclopentadienyl anion) with magnetic hysteresis up to 7.2 K (at 22 Oe/s magnetic sweep rate) where Er^{III} is solely coordinated by three Re^I ions.

Results and discussion

Synthetic strategy

ErRe₃ is obtained following the procedure reported by Kempe et al. for [Sm^{III}(Re^ICp₂)₃].³² [Er^{III}(btmsm)₃] (obtained according to literature procedures⁴¹⁻⁴²; btmsm = bis(trimethylsilyl)methyl anion) reacts with [Cp₂ReH]⁴³ in benzene (Figure 1D). The btmsm[−] ligand coordinated to Er^{III} acts as a strong base capable of deprotonating [Cp₂ReH] – a weak acid. Deprotonation of [Cp₂ReH] leads to the elimination of the bis(trimethylsilyl)methane by-product ('alkane elimination'¹³⁴) and the formation of anionic [Cp₂Re^I][−] species that readily coordinate to Er^{III} resulting in the formation of a trigonal planar complex [Er^{III}(Re^ICp₂)₃].

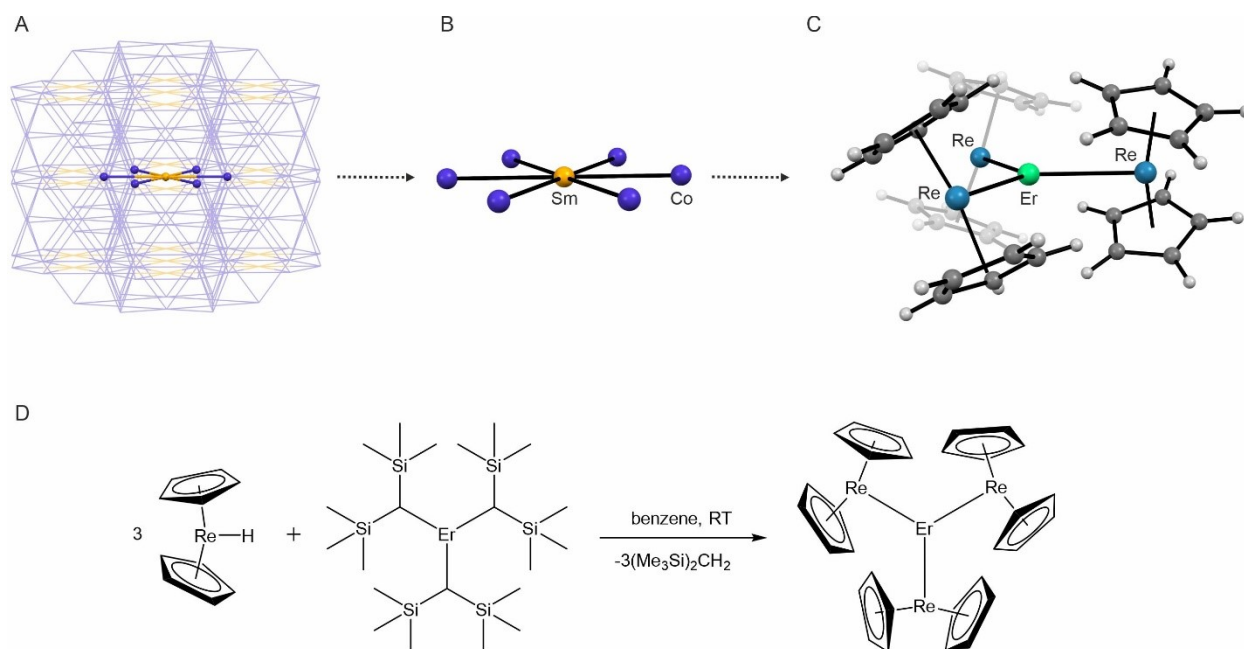


Figure 1. The synthetic strategy towards ErRe_3 and its structure.

Graphical representation of the structural design transfer from the intermetallic magnet SmCo_5 (A and B) to the molecular nanomagnet $[\text{Er}^{\text{III}}(\text{Re}^{\text{I}}\text{Cp}_2)_3]$ (C). The hexagonal planar SmCo_6 coordination with unsupported coordination bonds between the center of the rare earth and six transition metals in SmCo_5 (A and B) is mimicked by the trigonal planar coordination in ErRe_3 (C). All three panels A-C are based on single-crystal structural models of SmCo_5 ¹ and ErRe_3 . Sm-Co bonds in SmCo_5 : 2.888 Å; Er-Re bonds in ErRe_3 : 2.9004(5), 2.9124(5), 2.9172(5) Å. Panel D presents the synthesis of ErRe_3 based on the work of Kempe et al.³² This approach utilizes the reaction of the weak Brønsted acid $[\text{Cp}_2\text{ReH}]$ with the strong Brønsted base btmsm^- in $[\text{Er}^{\text{III}}(\text{btmsm})_3]$ resulting in $(\text{Me}_3\text{Si})_2\text{CH}_2$ "elimination" and the formation of $[\text{Er}^{\text{III}}(\text{Re}^{\text{I}}\text{Cp}_2)_3]$.

Crystal structure

ErRe_3 crystallizes slowly from benzene in the form of small yellow prism crystals which were characterized structurally by single-crystal X-ray diffraction (SCXRD; trigonal $R\bar{3}$; Table S1). The SCXRD structural analysis confirmed the coordination of three Re^{I} ions to the Er^{III} center with the formation of a nearly perfect trigonal planar neutral complex $[\text{Er}^{\text{III}}(\text{Re}^{\text{I}}\text{Cp}_2)_3]$ (Figure 1C) with the Re-Er-Re angles very close to 120° ($121.22(2)$, $119.15(2)$ and $119.62(2)^\circ$) and the Er atom lying only 0.013(1) Å above the Re_3 plane. The cyclopentadienyl ligands are coordinated solely to Re^{I} and arranged in a slightly tilted manner below and above the equatorial plane of the ErRe_3 molecule (Figure 1C). There are no other coordination bonds to Er^{III} . Other intramolecular contacts of Er^{III} involve Cp ligands with the shortest Er...C distances in the 2.829(8)-3.056(13) Å range – well beyond typical coordination bonds of lanthanide complexes. The Er-Re distances in ErRe_3 (2.9004(5), 2.9124(5) and 2.9172(5) Å) are similar to those reported for $[\text{Sm}^{\text{III}}(\text{Re}^{\text{I}}\text{Cp}_2)_3]$, $[\text{La}^{\text{III}}(\text{Re}^{\text{I}}\text{Cp}_2)_3]$ and $[\text{Lu}^{\text{III}}(\text{Re}^{\text{I}}\text{Cp}_2)_3]$ ³² as well as other molecular compounds with unsupported rare earth - transition metal bonds^{34, 38} and the intermetallic SmCo_5 with Sm-Co distances of 2.888 Å.¹ The comparison of the Re-Cp distances in ErRe_3 and the $[\text{Cp}_2\text{ReH}]$ starting material (SCXRD structural analysis of $[\text{Cp}_2\text{ReH}]$ was performed as part of this study Table S1; CCDC 2027573) confirms the change of the valence state of the Re centers upon coordination to Er^{III} . The slightly unsymmetrical and tilted $[\text{Cp}_2\text{ReH}]$ with the average Re-Cp_{centroid} distance of 1.877(44) Å is similar to other compounds of this type⁴⁴⁻⁴⁶ and shows slight

shortening of these contacts in **ErRe₃** to av. 1.864(8) Å (Figure S1). The [Er^{III}(Re^ICp₂)₃] molecules are stacked on top of each other in a hexagonal fashion along the *c* crystallographic direction, leading to the formation of channels filled with disordered benzene molecules (Figure S2). The shortest intermolecular distances between the Er^{III} centers can be found within the aforementioned stacks and amount to 7.6318(6) Å. There are six more nearest Er^{III} neighbors within the 10 Å radius with distances larger than 9 Å (Figure S3). This ensures sufficient magnetic isolation of the individual [Er^{III}(Re^ICp₂)₃] molecules taking into account that all intermolecular contacts are van der Waals in nature and do not transmit magnetic interactions efficiently. Before attempting the magnetic characterization **ErRe₃** was subjected to a rigorous purity verification by performing powder X-ray diffraction (PXRD) experiment for a sample loaded into a 0.3 mm glass capillary immersed in benzene and sealed using high vacuum grease (identical conditions were applied during the magnetic measurements discussed below). The experimental PXRD pattern shows very narrow peaks and matches almost perfectly the simulated one using 270 K SCXRD data (Figure S4).

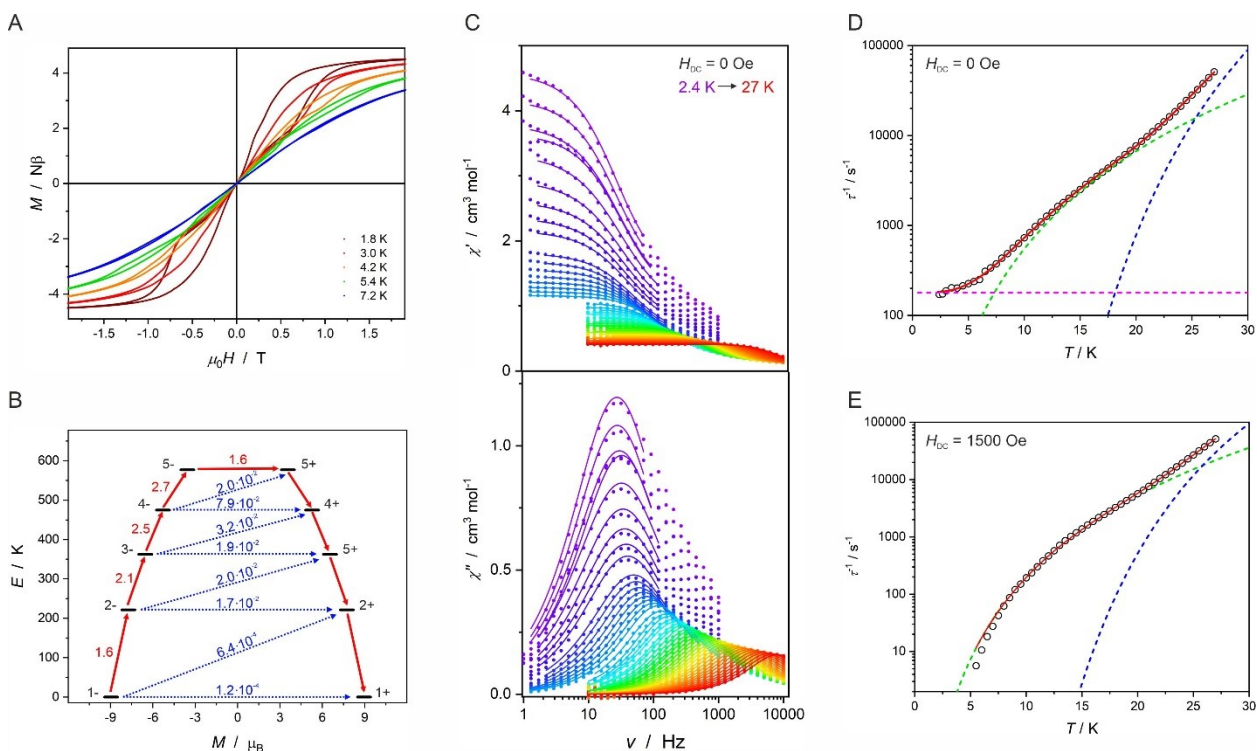


Figure 2. Magnetic properties of ErRe₃.

Magnetic hysteresis loops recorded with the 2.2 mT·s⁻¹ magnetic field sweep rate in the -2 to 2 T range (A). Energy of the calculated Kramers Doublets (KDs) arising from the splitting of the ⁴I_{15/2} multiplet of Er^{III} in **ErRe₃** with the most probable relaxation pathway represented by the red arrows (B). AC magnetic susceptibility recorded at zero magnetic field in the 2.4 – 27 K range, demonstrating the slow magnetization dynamics of **ErRe₃**, solid lines are the best fits to the generalized Debye model with parameters presented in Table S2 (C). Temperature dependence of the magnetization relaxation rate $\tau^{-1}(T)$ at zero (D) and 0.15 mT (E) magnetic field obtained from the generalized Debye fitting of the respective AC magnetic susceptibility measurements (circles – experimental points, red line – best fits using Eq. 1 (D) and Eq. 2 (E), blue dashed line – Orbach relaxation, green dashed line – Raman relaxation, magenta dashed line – QTM relaxation).

Magnetic properties

The unusual coordination environment of Er^{III} in **ErRe₃** may cast doubts on the nature of its electronic ground state. However, magnetic measurements for **ErRe₃** confirm the valence states of the central Er^{III} ion and the Re^I donor atoms. The χT (χ – molar magnetic susceptibility) value of 11.3 cm³·K·mol⁻¹ at 260 K is close to 11.48 cm³·K·mol⁻¹ expected for Er^{III} ⁴I_{15/2} ground multiplet (Figure S5). Similar agreement between the experiment and the expected χT was reported for [Sm^{III}(Re^ICp₂)₃] (⁶H_{5/2} multiplet).³² This is further confirmed by a very good agreement of the experimental χT and the *ab initio* calculations (red solid line in Figure S5 and supplemental information) using Molcas.^{47, 48} The $\chi T(T)$ dependence shows an abrupt increase below 18 K, which can be ascribed to ferromagnetic intermolecular interactions and blocking of magnetization.

The $M(H)$ (M – molar magnetization, H – magnetic field) measurements (magnetic field sweep rate of 2.2 mT·s⁻¹) revealed the presence of waist-restricted (pinched) magnetic hysteresis loops up to 7.2 K (Figure 2A), originating from the slow relaxation of the magnetization of the trigonal **ErRe₃**. This temperature matches Er^{III} sandwich and metallocene complexes.⁴⁹ Furthermore, the hysteresis loop in **ErRe₃** opens in the 0.05 – 1.5 T range at 1.8 K and is the widest among trigonal Er^{III} MNMs.

The slow magnetization dynamics were studied and confirmed by the alternating current (AC) magnetic susceptibility measurements performed in the 1-10000 Hz frequency range up to 27 K in the absence of the external magnetic field (Figure 2C and Table S2). However, the resulting temperature dependence of the magnetic relaxation rate $\tau^{-1}(T)$ (Figure 2D) contains contributions from three processes: quantum tunneling of magnetization (QTM), Orbach and Raman described by six parameters included in Equation 1:

$$\tau^{-1} = \frac{A_1}{1+A_2H^2} + CT^n + \tau_0^{-1} \exp\left(\frac{-U_{eff}}{k_B T}\right) \quad \text{Eq. 1}$$

hence, all relevant parameters: A_1 , A_2 , C , n , τ_0 and, most importantly, the effective energy barrier for the magnetization reversal arising from the Orbach relaxation cannot be extracted reliably from AC data collected at zero DC field. To mitigate this issue, the AC magnetic studies were repeated under an applied DC magnetic field of 0.15 T (Figure S6 and Table S3). The presence of a small applied magnetic field quenches the QTM with only negligible direct process, which was accurately determined from the magnetic field dependence of the relaxation time (Figure S7 and Table S4). Thus, the temperature dependence of the relaxation rate under $H_{DC} = 0.15$ T could be reliably fitted including only the Raman and Orbach relaxation mechanisms using Equation 2:

$$\tau^{-1} = CT^n + \tau_0^{-1} \exp\left(\frac{-U_{eff}}{k_B T}\right) \quad \text{Eq. 2}$$

where τ^{-1} is the magnetic relaxation rate, C and n parameters describe the Raman-like process, and τ_0 and U_{eff} are related to the Orbach process. The satisfactory fit could be obtained with $C = 0.0035(4)$ K^{- n} ·s⁻¹, $n = 4.74(3)$, $\tau_0 = 3.0(5) \cdot 10^{-10}$ s and $U_{eff} = 314(5)$ K with $R^2 = 0.99987$ (Figure 2E).

The obtained effective energy barrier for the magnetization reversal $U_{eff} = 314(5)$ K is significantly smaller than expected from the theoretical calculations (CASSCF-RASSI; OpenMolcas 19.11⁴⁷; for details see Supplemental Information including Tables S5 and S6 with the information on basis sets, spin-orbit energies and g -tensors of the lowest Kramers Doublets, respectively), predicting the fastest relaxation

between the $5\pm$ Kramers Doublet lying 576 K above the highly axial ground state (Figure 2B and Table S6). The value 314(5) K is therefore underestimated. Additional fittings of the Raman and Orbach processes with fixed U_{eff} values corresponding to the calculated energies of the lower KDs were performed: $2\pm$ of 224 K, $3\pm$ of 363 K and $4\pm$ of 475 K. The best fits (Figures S8A-S8C) are characterized by the following R^2 values: 0.99702 for $U_{\text{eff } 2\pm} = 224$ K, 0.99960 for $U_{\text{eff } 3\pm} = 363$ K and 0.99808 for $U_{\text{eff } 4\pm} = 475$ K. The best agreement is clearly observed for $U_{\text{eff } 3\pm} = 363$ K, which corresponds to the energy of the third KD. This is also closest to the value obtained from the free fitting of the relaxation processes presented in Figure 2E. An attempt to describe the magnetic relaxation of **ErRe₃** using only the Raman-like process leads to a very poor fit as depicted in Figure S8D. Thus we conclude, that the observed Orbach relaxation for **ErRe₃** proceeds predominantly through the third Kramers Doublet, characterized by the estimated energy barrier U_{eff} approaching 363 K. This value is three times higher than that observed for the best trigonal^{42, 50} or low-coordinate^{51, 52} Er^{III} molecules and is comparable to the Er^{III} sandwich and metallocene complexes.^{37, 49, 53-57} Interestingly, **ErRe₃** shows significantly slower relaxation as compared to $[\text{Er}(\text{N}(\text{SiMe}_3)_2)_3]$ characterized by $U_{\text{eff}} = 122$ K⁵⁰ and surpasses the theoretical limit of 306 K (212.6 cm^{-1}) for any trigonal planar molecule based on the theoretical analysis of a hypothetical $\text{Er}^{\text{III}}(\text{NH}_2)_3$ compound.⁵⁸ **ErRe₃** is a clear demonstration that direct bonding of transition metals to lanthanides might be one of the most promising directions towards room temperature MNMs, especially if paramagnetic donor atoms could be used.

Experimental procedures

Resource availability

Lead contact

Further information and requests for resources should be directed to and will be fulfilled by the lead contact, Dawid Pinkowicz (dawid.pinkowicz@uj.edu.pl).

Materials availability

This study did not generate new unique reagents.

Data and code availability

Crystallographic data for this paper (**ErRe₃** at 100 K: CCDC 2065530, **ErRe₃** at 270 K: CCDC 2065531 and $[\text{Cp}_2\text{ReH}]$ at 100 K: CCDC 2027573) were deposited with the Cambridge Structural Database and can be obtained free of charge from the Cambridge Crystallographic Data Centre via www.ccdc.cam.ac.uk/data_request/cif. All other data are available from the lead contact without restriction.

Preparation of $[\text{Er}^{\text{III}}(\text{Re}^{\text{I}}\text{Cp}_2)_3] \cdot 0.5\text{C}_6\text{H}_6$ (**ErRe₃**)

All manipulations were performed in an argon-filled glovebox (Inert PureLab HE). $[\text{Cp}_2\text{ReH}]$ (242 mg; 0.76 mmol) was dissolved in anhydrous benzene (3.5 ml) and added to the benzene solution (2.5 ml) of $[\text{Er}^{\text{III}}(\text{btmsm})_3]$ (160 mg; 0.25 mmol). The resulting orange solution was stirred using a glass rod for 5 min and then stored in a 20 ml scintillation vial that was left open for 5 h inside the glovebox. After this time yellow-orange crystals appeared which were collected by vacuum filtration using a $1 \mu\text{m}$ Teflon membrane. Yield: 70 mg (0.061 mmol; 24%). The purity of the compound was checked by powder X-ray diffraction with the experimental pattern (Figure S4) matching nearly perfectly the simulated one from the

SCXRD structural model obtained at 270 K (CCDC 2065531). IR, neat (cm^{-1}): 796s, 808s, 816s, 832m, 850m, 987s, 1000s, 1059m, 1087s, 1095vs, 1154vw, 1188vw, 1201vw, 1255m, 1273m, 1342m, 1358m, 1394s, 1419s, 1462m, 1479m, 1558s, 1657s, 2001vw, 2034vw, 2854s, 2929vs, 3036m, 3063s, 3089s, 3550b (Figure S9).

Additional experimental and computational details

The relevant information is provided in the supplemental information.

Supplemental Information

List of items in the supplemental information attached at the end of the article:

Description of the experimental and computational details including general synthetic considerations, details of single crystal X-ray diffraction, details of powder X-ray diffraction, details of infrared spectroscopy, description of magnetic measurements and details of *ab initio* calculation.

Table S1. Selected crystallographic parameters for **ErRe₃** at 100 and 270 K and the starting material [**Cp₂Re^{III}H**] at 100 K.

Figure S1. Structural diagrams showing the asymmetric units (ASUs) of the starting material [**Cp₂Re^{III}H**] (A) and the target compound **ErRe₃** (B). The red numbers indicate the distances (Å) between the Re atoms and the centroids of the cyclopentadienyl rings. C – grey, H – light grey, Re – blue, Er – green, centroids – white; ellipsoids at the 40 % probability level for A and 30% for B.

Figure S2. Structural diagram of **ErRe₃** as viewed along the *c* crystallographic direction showing the hexagonal packing pattern of the [**Er^{III}(Re^ICp₂)₃**] molecules highlighted by red dotted hexagons. This type of packing leads to the formation of channels along the *c* axis filled with benzene molecules (crystallization solvent). Cyclopentadienyl ligands and benzene molecules are represented by black sticks and H-atoms are omitted for clarity.

Figure S3. Structural diagram demonstrating and listing Er...Er distances between all **ErRe₃** nearest neighbours. The shortest distance is 7.6318(6) Å along the *c* crystallographic direction.

Figure S4. Experimental (red line) and simulated (black line) powder X-ray diffraction experiments for **ErRe₃**. The simulated pattern is calculated based on the 270 K single crystal X-ray diffraction structural model and includes the contribution of the Cu Kβ which is observed in the experimental pattern.

Figure S5. Temperature dependence of the molar magnetic susceptibility and temperature product $\chi T(T)$ for **ErRe₃** recorded at $\mu_0 H = 0.1$ T (black points). The solid red line presents the $\chi T(T)$ obtained from the *ab initio* calculations (see text for details). The observed anomaly below 20 K is caused by the magnetization blocking and the ferromagnetic interactions between the neighbouring **ErRe₃** molecules.

Table S2. Results of the generalized Debye model fitting of the frequency dependence of the AC magnetic susceptibility χ' and χ'' for **ErRe₃** recorded at zero magnetic field in the 5.5 – 27 K range presented in Figure 2C (main text).

Figure S6. Frequency dependence of the AC magnetic susceptibility χ' and χ'' for **ErRe₃** recorded at $H_{DC} = 0.15$ T in the 5.5 – 27 K range using Quantum Design MPMS3 and PPMS instruments. Solid lines are the best fits to the generalized Debye model. The relevant fitting parameters can be found in Table S3 below.

Table S3. Results of the generalized Debye model fitting of the frequency dependence of the AC magnetic susceptibility χ' and χ'' for **ErRe₃** recorded at $H_{DC} = 0.15$ T in the 5.5 – 27 K range presented in Figure S6.

Figure S7. Frequency dependence of the AC magnetic susceptibility χ' and χ'' for **ErRe₃** recorded at $T = 7$ K in the 0.01 – 2 T range using Quantum Design MPMS3 and PPMS instruments. Solid lines are the best fits to the generalized Debye model. The relevant fitting parameters can be found in Table S4 below.

Table S4. Results of the generalized Debye model fitting of the frequency dependence of the AC magnetic susceptibility χ' and χ'' for **ErRe₃** recorded at $T = 7$ K in the 0.01 – 2 T range presented in Figure S6.

Table S5. The employed basis sets for *ab initio* calculations.

Table S6. Spin-orbit energies (cm⁻¹) and the *g*-tensors of the four lowest in energy Kramers doublets.

Figure S8. Temperature dependence of the magnetic relaxation rate $\tau^{-1}(T)$ for **ErRe₃** under applied 0.15 T DC magnetic field (circles). Solid lines represent the best fits assuming Raman-like and Orbach relaxation processes with C , n , τ_0 as free parameters and U_{eff} fixed at 224 K (A), 363 K (B), 475 K (C) or Raman-like relaxation process only (D). Fitting presented in B shows highest R^2 and is assumed to provide the most accurate value of the energy barrier for magnetization reversal. Fitting assuming Raman-like relaxation only (D) shows the lowest R^2 which sanctions the need for including the Orbach mechanism.

Figure S9. IR spectra of crushed crystals of **ErRe₃** (red solid line) with the overlaid IR spectrum of **SmRe₃** recorded as KBr pellet (black solid line) reproduced from ref. S13 in the 675-4000 cm⁻¹ range (the IR spectrum from Fig. S6 from the Supplementary Information of ref. S13 was traced using CorelDRAW 2019 software). Both spectra are very similar. Weak Re-H stretching modes at 2001 and 2034 cm⁻¹ observed for **ErRe₃** are due to the slight decomposition of this extremely sensitive compound. Note, that these stretches are also present in the IR spectrum of **SmRe₃**, but are largely obstructed by a significant background reaching 40% transmittance at 2000 cm⁻¹ and nearly 15% transmittance at 4000 cm⁻¹.

List of references in the supplemental information

Acknowledgments

This work was financed by the Polish National Science Centre within the Sonata Bis 6 project (2016/22/E/ST5/00055). The research was partially carried out with the equipment purchased thanks to the financial support of the European Regional Development Fund in the framework of the Smart Growth Operational Programme 2014-2020 (contract no. POIR.04.02.00-00-D001/20-00).

Author contributions

M.M. prepared the starting material [Cp₂ReH], participated in the preparation of the target compound, performed and analysed the magnetic measurements and wrote the relevant fragment of the manuscript; M.B. prepared the starting material [Er^{III}(btmsm)], participated in the preparation of the target compound, analysed its structure and wrote a relevant fragment of the manuscript; S.B. participated in the AC magnetic measurements and their analysis. V.V. performed and analysed the *ab initio* calculations and wrote the relevant fragment of the manuscript. D.P. acquired funding, designed the experiments, performed the synthesis of the target compound, coordinated and supervised the research and wrote the manuscript. All authors reviewed and agreed to the final version of the paper.

Declaration of interests

The authors declare no competing interests.

References

1. K. H. J. Buschow and A. S. Van Der Goot. Intermetallic compounds in the system samarium-cobalt. *Journal of the Less Common Metals*, **1968**, *14*, 323-328.
2. J. F. Herbst, J. J. Croat, F. E. Pinkerton and W. B. Yelon. Relationships between crystal structure and magnetic properties in Nd₂Fe₁₄B. *Physical Review B*, **1984**, *29*, 4176-4178.
3. J. J. Croat, J. F. Herbst, R. W. Lee and F. E. Pinkerton. High-energy product Nd-Fe-B permanent magnets. *Applied Physics Letters*, **1984**, *44*, 148-149.

4. O. Gutfleisch, M. A. Willard, E. Brück, C. H. Chen, S. G. Sankar and J. P. Liu. Magnetic Materials and Devices for the 21st Century: Stronger, Lighter, and More Energy Efficient. *Advanced Materials*, **2011**, 23, 821-842.
5. D. Gatteschi, R. Sessoli and J. Villain, *Molecular Nanomagnets*, 2006.
6. C. A. P. Goodwin, F. Ortu, D. Reta, N. F. Chilton and D. P. Mills. Molecular magnetic hysteresis at 60 kelvin in dysprosocenium. *Nature*, **2017**, 548, 439-442.
7. F.-S. Guo, B. M. Day, Y.-C. Chen, M.-L. Tong, A. Mansikkamäki and R. A. Layfield. Magnetic hysteresis up to 80 kelvin in a dysprosium metallocene single-molecule magnet. *Science*, **2018**, 362, 1400-1403.
8. C. A. Gould, K. R. McClain, J. M. Yu, T. J. Groshens, F. Furche, B. G. Harvey and J. R. Long. Synthesis and Magnetism of Neutral, Linear Metallocene Complexes of Terbium(II) and Dysprosium(II). *Journal of the American Chemical Society*, **2019**, 141, 12967-12973.
9. F.-S. Guo, B. M. Day, Y.-C. Chen, M.-L. Tong, A. Mansikkamäki and R. A. Layfield. A Dysprosium Metallocene Single-Molecule Magnet Functioning at the Axial Limit. *Angewandte Chemie International Edition*, **2017**, 56, 11445-11449.
10. K. Randall McClain, C. A. Gould, K. Chakarawet, S. J. Teat, T. J. Groshens, J. R. Long and B. G. Harvey. High-temperature magnetic blocking and magneto-structural correlations in a series of dysprosium(iii) metallocenium single-molecule magnets. *Chemical Science*, **2018**, 9, 8492-8503.
11. S.-G. Wu, Z.-Y. Ruan, J.-Y. Zheng, G.-Z. Huang, V. Vieru, Y.-C. Chen, L. T. A. Ho, J.-L. Liu, L. F. Chibotaru and M.-L. Tong. Rectangle-like hysteresis in a Dysprosium Metallocrown Magnet with Linear F-Dy-F Anisotropic Moiety. *arXiv*, **2021**, DOI: arXiv:2105.09586.
12. D. Yan, C. Joana, R. Lorena, C. Salvador, J. B. José and G.-A. Alejandro. Data mining, dashboards and statistics: a powerful framework for the chemical design of molecular nanomagnets. *Research Square*, **2021**, DOI: 10.21203/rs.3.rs-490959/v1.
13. J.-L. Liu, Y.-C. Chen and M.-L. Tong. Symmetry strategies for high performance lanthanide-based single-molecule magnets. *Chemical Society Reviews*, **2018**, 47, 2431-2453.
14. N. Ishikawa, M. Sugita, T. Ishikawa, S.-y. Koshihara and Y. Kaizu. Lanthanide Double-Decker Complexes Functioning as Magnets at the Single-Molecular Level. *Journal of the American Chemical Society*, **2003**, 125, 8694-8695.
15. J. D. Rinehart and J. R. Long. Exploiting single-ion anisotropy in the design of f-element single-molecule magnets. *Chemical Science*, **2011**, 2, 2078-2085.
16. D. Reta, J. G. C. Kragoskow and N. F. Chilton. Ab Initio Prediction of High-Temperature Magnetic Relaxation Rates in Single-Molecule Magnets. *Journal of the American Chemical Society*, **2021**, 143, 5943-5950.
17. M. Briganti, F. Santanni, L. Tesi, F. Totti, R. Sessoli and A. Lunghi. A Complete Ab Initio View of Orbach and Raman Spin–Lattice Relaxation in a Dysprosium Coordination Compound. *Journal of the American Chemical Society*, **2021**, 143, 13633-13645.
18. C. E. Jackson, I. P. Moseley, R. Martinez, S. Sung and J. M. Zadrozny. A reaction-coordinate perspective of magnetic relaxation. *Chemical Society Reviews*, **2021**, 50, 6684-6699.
19. K. L. M. Harriman and M. Murugesu. An Organolanthanide Building Block Approach to Single-Molecule Magnets. *Accounts of Chemical Research*, **2016**, 49, 1158-1167.
20. S.-G. Wu, Z.-Y. Ruan, G.-Z. Huang, J.-Y. Zheng, V. Vieru, G. Taran, J. Wang, Y.-C. Chen, J.-L. Liu, L. T. A. Ho, L. F. Chibotaru, W. Wernsdorfer, X.-M. Chen and M.-L. Tong. Field-induced oscillation of magnetization blocking barrier in a holmium metallocrown single-molecule magnet. *Chem*, **2021**, 7, 982-992.
21. P. Evans, D. Reta, G. F. S. Whitehead, N. F. Chilton and D. P. Mills. Bis-Monophospholyl Dysprosium Cation Showing Magnetic Hysteresis at 48 K. *Journal of the American Chemical Society*, **2019**, 141, 19935-19940.

22. J. P. Durrant, J. Tang, A. Mansikkamäki and R. A. Layfield. Enhanced single-molecule magnetism in dysprosium complexes of a pristine cyclobutadienyl ligand. *Chemical Communications*, **2020**, 56, 4708-4711.
23. C. J. Milios, A. Vinslava, W. Wernsdorfer, S. Moggach, S. Parsons, S. P. Perlepes, G. Christou and E. K. Brechin. A Record Anisotropy Barrier for a Single-Molecule Magnet. *Journal of the American Chemical Society*, **2007**, 129, 2754-2755.
24. K. Qian, X.-C. Huang, C. Zhou, X.-Z. You, X.-Y. Wang and K. R. Dunbar. A Single-Molecule Magnet Based on Heptacyanomolybdate with the Highest Energy Barrier for a Cyanide Compound. *Journal of the American Chemical Society*, **2013**, 135, 13302-13305.
25. T. Lis. Preparation, structure, and magnetic properties of a dodecanuclear mixed-valence manganese carboxylate. *Acta Crystallographica Section B*, **1980**, 36, 2042-2046.
26. R. Sessoli, H. L. Tsai, A. R. Schake, S. Wang, J. B. Vincent, K. Folting, D. Gatteschi, G. Christou and D. N. Hendrickson. High-spin molecules: [Mn₁₂O₁₂(O₂CR)₁₆(H₂O)₄]. *Journal of the American Chemical Society*, **1993**, 115, 1804-1816.
27. R. Sessoli, D. Gatteschi, A. Caneschi and M. A. Novak. Magnetic bistability in a metal-ion cluster. *Nature*, **1993**, 365, 141-143.
28. M. He, F.-S. Guo, J. Tang, A. Mansikkamäki and R. A. Layfield. Fulvalene as a platform for the synthesis of a dimetallic dysprosocenium single-molecule magnet. *Chemical Science*, **2020**, 11, 5745-5752.
29. M. He, F.-S. Guo, J. Tang, A. Mansikkamäki and R. A. Layfield. Synthesis and single-molecule magnet properties of a trimetallic dysprosium metallocene cation. *Chemical Communications*, **2021**, 57, 6396-6399.
30. P. Evans, D. Reta, C. A. P. Goodwin, F. Ortu, N. F. Chilton and D. P. Mills. A double-dysprosocenium single-molecule magnet bound together with neutral ligands. *Chemical Communications*, **2020**, 56, 5677-5680.
31. J. Liu, J. Li, Z. Xu, X. Zhou, Q. Xue, T. Wu, M. Zhong, R. Li, R. Sun, Z. Shen, H. Tang, S. Gao, B. Wang, S. Hou and Y. Wang. On-surface preparation of coordinated lanthanide-transition-metal clusters. *Nature Communications*, **2021**, 12, 1619.
32. M. V. Butovskii, C. Döring, V. Bezugly, F. R. Wagner, Y. Grin and R. Kempe. Molecules containing rare-earth atoms solely bonded by transition metals. *Nature Chemistry*, **2010**, 2, 741-744.
33. K. Shi, I. Douair, G. Feng, P. Wang, Y. Zhao, L. Maron and C. Zhu. Heterometallic Clusters with Multiple Rare Earth Metal–Transition Metal Bonding. *Journal of the American Chemical Society*, **2021**, 143, 5998-6005.
34. M. V. Butovskii, O. L. Tok, F. R. Wagner and R. Kempe. Bismetallocenes: Lanthanoid–Transition-Metal Bonds through Alkane Elimination. *Angewandte Chemie International Edition*, **2008**, 47, 6469-6472.
35. A. Swain, A. Sen and G. Rajaraman. Are lanthanide-transition metal direct bonds a route to achieving new generation {3d–4f} SMMs? *Dalton Transactions*, **2021**, 50, 16099-16109.
36. C. A. Gould, K. R. McClain, D. Reta, J. G. C. Kragoskow, D. A. Marchiori, E. Lachman, E.-S. Choi, J. G. Analytis, R. D. Britt, N. F. Chilton, B. G. Harvey and J. R. Long. Ultrahard magnetism from mixed-valence dilanthanide complexes with metal–metal bonding. *Science*, **2022**.
37. J. J. Le Roy, L. Ungur, I. Korobkov, L. F. Chibotaru and M. Murugesu. Coupling Strategies to Enhance Single-Molecule Magnet Properties of Erbium–Cyclooctatetraenyl Complexes. *Journal of the American Chemical Society*, **2014**, 136, 8003-8010.
38. C. P. Burns, X. Yang, J. D. Wofford, N. S. Bhuvanesh, M. B. Hall and M. Nippe. Structure and Magnetization Dynamics of Dy–Fe and Dy–Ru Bonded Complexes. *Angewandte Chemie International Edition*, **2018**, 57, 8144-8148.

39. L. Münzfeld, X. Sun, S. Schlittenhardt, C. Schoo, A. Hauser, S. Gillhuber, F. Weigend, M. Ruben and P. W. Roesky. Introduction of plumbale to f-element chemistry. *Chemical Science*, **2022**, DOI: 10.1039/D1SC03805B.
40. P. Zhang, F. Benner, N. F. Chilton and S. Demir. Organometallic lanthanide bismuth cluster single-molecule magnets. *Chem*, **2021**, DOI: <https://doi.org/10.1016/j.chempr.2021.11.007>.
41. A. G. Avent, C. F. Caro, P. B. Hitchcock, M. F. Lappert, Z. Li and X.-H. Wei. Synthetic and structural experiments on yttrium, cerium and magnesium trimethylsilylmethyls and their reaction products with nitriles; with a note on two cerium β -diketiminates. *Dalton Transactions*, **2004**, DOI: 10.1039/B316695N, 1567-1577.
42. H. Zhang, R. Nakanishi, K. Katoh, B. K. Breedlove, Y. Kitagawa and M. Yamashita. Low coordinated mononuclear erbium(iii) single-molecule magnets with C_{3v} symmetry: a method for altering single-molecule magnet properties by incorporating hard and soft donors. *Dalton Transactions*, **2018**, 47, 302-305.
43. M. L. H. Green, L. Pratt and G. Wilkinson. 795. Biscyclopentadienylrhenium hydride. *Journal of the Chemical Society (Resumed)*, **1958**, DOI: 10.1039/JR9580003916, 3916-3922.
44. C. Apostolidis, B. Kanellakopulos, R. Maier, J. Rebizant and M. L. Ziegler. Bis(cyclopentadienyl)rhenium(III)chloride: Kristallstruktur, Eigenschaften und Reaktivität; Darstellung und Charakterisierung von Cp₃Re und Cp₂ReH. *Journal of Organometallic Chemistry*, **1991**, 409, 243-254.
45. R. A. Paciello, P. Kiprof, E. Herdtweck and W. A. Herrmann. Synthesis and structural characterization of a mixed-ring rhenocene hydride complex, (η^5 -5-cyclopentadienyl)(η^5 -5-pentamethylcyclopentadienyl)hydridorhenium. *Inorganic Chemistry*, **1989**, 28, 2890-2893.
46. J. A. Bandy, F. G. N. Cloke, G. Copper, J. P. Day, R. B. Girling, R. G. Graham, J. C. Green, R. Grinter and R. N. Perutz. Decamethylrhenocene, (η^5 -C₅Me₅)₂Re. *Journal of the American Chemical Society*, **1988**, 110, 5039-5050.
47. F. Aquilante, J. Autschbach, A. Baiardi, S. Battaglia, V. A. Borin, L. F. Chibotaru, I. Conti, L. D. Vico, M. Delcey, I. F. Galván, N. Ferré, L. Freitag, M. Garavelli, X. Gong, S. Knecht, E. D. Larsson, R. Lindh, M. Lundberg, P. Å. Malmqvist, A. Nenov, J. Norell, M. Odelius, M. Olivucci, T. B. Pedersen, L. Pedraza-González, Q. M. Phung, K. Pierloot, M. Reiher, I. Schapiro, J. Segarra-Martí, F. Segatta, L. Seijo, S. Sen, D.-C. Sergentu, C. J. Stein, L. Ungur, M. Vacher, A. Valentini and V. Veryazov. Modern quantum chemistry with [Open]Molcas. *The Journal of Chemical Physics*, **2020**, 152, 214117.
48. L. F. Chibotaru and L. Ungur. Ab initio calculation of anisotropic magnetic properties of complexes. I. Unique definition of pseudospin Hamiltonians and their derivation. *The Journal of Chemical Physics*, **2012**, 137, 064112.
49. S.-M. Chen, J. Xiong, Y.-Q. Zhang, Q. Yuan, B.-W. Wang and S. Gao. A soft phosphorus atom to "harden" an erbium(iii) single-ion magnet. *Chemical Science*, **2018**, 9, 7540-7545.
50. P. Zhang, L. Zhang, C. Wang, S. Xue, S.-Y. Lin and J. Tang. Equatorially Coordinated Lanthanide Single Ion Magnets. *Journal of the American Chemical Society*, **2014**, 136, 4484-4487.
51. M. Brzozowska, G. Handzlik, K. Kurpiewska, M. Zychowicz and D. Pinkowicz. Pseudo-tetrahedral vs. pseudo-octahedral ErIII single molecule magnets and the disruptive role of coordinated TEMPO radical. *Inorganic Chemistry Frontiers*, **2021**, 8, 2817-2828.
52. A. J. Brown, D. Pinkowicz, M. R. Saber and K. R. Dunbar. A Trigonal-Pyramidal Erbium(III) Single-Molecule Magnet. *Angewandte Chemie International Edition*, **2015**, 54, 5864-5868.
53. L. Münzfeld, C. Schoo, S. Bestgen, E. Moreno-Pineda, R. Köppe, M. Ruben and P. W. Roesky. Synthesis, structures and magnetic properties of [(η^9 -C₉H₉)Ln(η^8 -C₈H₈)] super sandwich complexes. *Nature Communications*, **2019**, 10, 3135.
54. S.-D. Jiang, B.-W. Wang, H.-L. Sun, Z.-M. Wang and S. Gao. An Organometallic Single-Ion Magnet. *Journal of the American Chemical Society*, **2011**, 133, 4730-4733.

55. K. R. Meihaus and J. R. Long. Magnetic Blocking at 10 K and a Dipolar-Mediated Avalanche in Salts of the Bis(η^8 -cyclooctatetraenide) Complex $[\text{Er}(\text{COT})_2]^-$. *Journal of the American Chemical Society*, **2013**, *135*, 17952-17957.
56. J. J. Le Roy, I. Korobkov and M. Murugesu. A sandwich complex with axial symmetry for harnessing the anisotropy in a prolate erbium(iii) ion. *Chemical Communications*, **2014**, *50*, 1602-1604.
57. Y.-S. Meng, C.-H. Wang, Y.-Q. Zhang, X.-B. Leng, B.-W. Wang, Y.-F. Chen and S. Gao. (Boratabenzene)(cyclooctatetraenyl) lanthanide complexes: a new type of organometallic single-ion magnet. *Inorganic Chemistry Frontiers*, **2016**, *3*, 828-835.
58. F. Lu, M.-M. Ding, J.-X. Li, B.-L. Wang and Y.-Q. Zhang. Why lanthanide ErIII SIMs cannot possess huge energy barriers: a theoretical investigation. *Dalton Transactions*, **2020**, *49*, 14576-14583.

Supplemental Information

Table of contents

Description of the experimental and computational details including general synthetic considerations, details of single crystal X-ray diffraction, details of powder X-ray diffraction, details of infrared spectroscopy, description of magnetic measurements and details of *ab initio* calculation.

Table S1. Selected crystallographic parameters for **ErRe₃** at 100 and 270 K and the starting material [Cp₂Re^{III}H] at 100 K.

Figure S1. Structural diagrams showing the asymmetric units (ASUs) of the starting material [Cp₂Re^{III}H] (A) and the target compound **ErRe₃** (B). The red numbers indicate the distances (Å) between the Re atoms and the centroids of the cyclopentadienyl rings. C – grey, H – light grey, Re – blue, Er – green, centroids – white; ellipsoids at the 40 % probability level for A and 30% for B.

Figure S2. Structural diagram of **ErRe₃** as viewed along the *c* crystallographic direction showing the hexagonal packing pattern of the [Er^{III}(Re^ICp₂)₃] molecules highlighted by red dotted hexagons. This type of packing leads to the formation of channels along the *c* axis filled with benzene molecules (crystallization solvent). Cyclopentadienyl ligands and benzene molecules are represented by black sticks and H-atoms are omitted for clarity.

Figure S3. Structural diagram demonstrating and listing Er...Er distances between all **ErRe₃** nearest neighbours. The shortest distance is 7.6318(6) Å along the *c* crystallographic direction.

Figure S4. Experimental (red line) and simulated (black line) powder X-ray diffraction experiments for **ErRe₃**. The simulated pattern is calculated based on the 270 K single crystal X-ray diffraction structural model and includes the contribution of the Cu Kβ which is observed in the experimental pattern.

Figure S5. Temperature dependence of the molar magnetic susceptibility and temperature product $\chi T(T)$ for **ErRe₃** recorded at $\mu_0 H = 0.1$ T (black points). The solid red line presents the $\chi T(T)$ obtained from the *ab initio* calculations (see text for details). The observed anomaly below 20 K is caused by the magnetization blocking and the ferromagnetic interactions between the neighbouring **ErRe₃** molecules.

Table S2. Results of the generalized Debye model fitting of the frequency dependence of the AC magnetic susceptibility χ' and χ'' for **ErRe₃** recorded at zero magnetic field in the 5.5 – 27 K range presented in Figure 2C (main text).

Figure S6. Frequency dependence of the AC magnetic susceptibility χ' and χ'' for **ErRe₃** recorded at $H_{DC} = 0.15$ T in the 5.5 – 27 K range using Quantum Design MPMS3 and PPMS instruments. Solid lines are the best fits to the generalized Debye model. The relevant fitting parameters can be found in Table S3 below.

Table S3. Results of the generalized Debye model fitting of the frequency dependence of the AC magnetic susceptibility χ' and χ'' for **ErRe₃** recorded at $H_{DC} = 0.15$ T in the 5.5 – 27 K range presented in Figure S6.

Figure S7. Frequency dependence of the AC magnetic susceptibility χ' and χ'' for **ErRe₃** recorded at $T = 7$ K in the 0.01 – 2 T range using Quantum Design MPMS3 and PPMS instruments. Solid lines are the best fits to the generalized Debye model. The relevant fitting parameters can be found in Table S4 below.

Table S4. Results of the generalized Debye model fitting of the frequency dependence of the AC magnetic susceptibility χ' and χ'' for **ErRe₃** recorded at $T = 7$ K in the 0.01 – 2 T range presented in Figure S6.

Table S5. The employed basis sets for *ab initio* calculations.

Table S6. Spin-orbit energies (cm^{-1}) and the g -tensors of the four lowest in energy Kramers doublets.

Figure S8. Temperature dependence of the magnetic relaxation rate $\tau^{-1}(T)$ for **ErRe₃** under applied 0.15 T DC magnetic field (circles). Solid lines represent the best fits assuming Raman-like and Orbach relaxation processes with C , n , τ_0 as free parameters and U_{eff} fixed at 224 K (A), 363 K (B), 475 K (C) or Raman-like relaxation process only (D). Fitting presented in B shows highest R^2 and is assumed to provide the most accurate value of the energy barrier for magnetization reversal. Fitting assuming Raman-like relaxation only (D) shows the lowest R^2 which sanctions the need for including the Orbach mechanism.

Figure S9. IR spectra of crushed crystals of **ErRe₃** (red solid line) with the overlaid IR spectrum of **SmRe₃** recorded as KBr pellet (black solid line) reproduced from ref. S13 in the 675-4000 cm^{-1} range (the IR spectrum from Fig. S6 from the Supplementary Information of ref. S13 was traced using CorelDRAW 2019 software). Both spectra are very similar. Weak Re-H stretching modes at 2001 and 2034 cm^{-1} observed for **ErRe₃** are due to the slight decomposition of this extremely sensitive compound. Note, that these stretches are also present in the IR spectrum of **SmRe₃**, but are largely obstructed by a significant background reaching 40% transmittance at 2000 cm^{-1} and nearly 15% transmittance at 4000 cm^{-1} .

List of references in the supplemental information

Experimental and computational details

General synthetic considerations

All manipulations were performed under argon gas atmosphere inside Inert PureLab HE glovebox ($O_2 < 0.1$ ppm and $H_2O < 0.5$ ppm). All solvents used in this study (except benzene) were of HPLC grade and were additionally dried under argon using Inert PureSolv EN7 solvent purification system and stored over molecular sieves for more than 24 h prior to use. Anhydrous benzene was purchased from commercial sources (Merck) and degassed prior to use by performing three freeze-pump-thaw cycles prior to use. Anhydrous $ReCl_5$ (at least 99.9%) was purchased from Merck and used as received for the preparation of $[Cp_2ReH]$ according to the literature procedure (ref. S1). $[Er^{III}(btmsm)_3]$ was also prepared according to the literature procedures (refs. S2 and S3).

Details of single crystal X-ray diffraction (SCXRD)

SCXRD measurements were performed using Bruker D8 Quest Eco diffractometer equipped with Photon II CPAD detector, $MoK\alpha$ sealed tube radiation source and Triumph[®] optics. The SCXRD experimental details can be found in Table S1 and in the respective crystallographic information files (cif) deposited with the Cambridge Crystallographic Data Centre accessible free of charge via www.ccdc.cam.ac.uk/data_request/cif: CCDC 2065530 (**ErRe₃** at 100 K), CCDC 2065531 (**ErRe₃** at 270 K) and CCDC 2027573 ($[Cp_2ReH]$ at 100 K). The single crystals were removed from the mother liquor directly into the Type NVH Cargille Immersion Oil and mounted using a 100 μm MiTeGen cryoloop. The data collections were performed at 100 K for **ErRe₃** and $[Cp_2ReH]$ and then again for **ErRe₃** at 270 K for comparison with the experimental PXRD pattern of the bulk sample of **ErRe₃**. Data processing was performed using Apex4 suite of programs – the details can be found in the cif files. The structures were solved using direct methods and refined anisotropically (weighted full-matrix least-squares on F^2 , refs. S4 and S5). Hydrogen atoms were placed in the calculated positions and refined as riding on the parent atoms. Structural diagrams were prepared using Mercury 2020.2.0 software (CCDC) and CorelDRAW 2019.

Details of powder X-ray diffraction (PXRD)

PXRD pattern for **ErRe₃** was collected using Bruker D8 Advance Eco diffractometer equipped with Lynxeye silicon strip detector, Cu sealed tube radiation source and capillary stage. A sample of **ErRe₃** was ground to a fine powder using an agate mortar inside the glovebox and loaded into a glass capillary 0.3 mm in diameter. The capillary was broken in half inside the glovebox and the open end was sealed using silicon grease before it was moved to the PXRD instrument and mounted on the goniometer head using bee wax. The PXRD pattern was collected in 27 consecutive scans (12 minutes each) in the 3-50 2θ range to exclude the possibility of the decomposition of the sample. No signs of decomposition within the experiment time were observed: the first and the last scans are identical. The experimental PXRD pattern is presented in Figure S4 (red line) and compared against the simulated curve (gray line) obtained from the SCXRD data collected at 270 K (the simulated curves, that include the $CuK\beta$ component were exported using Mercury 2020.2.0 software).

Details of infrared spectroscopy (IR)

IR spectra were collected using Nicolet iN10 MX FT-IR microscope in the transmission mode. A small powdered sample of **ErRe₃** was placed on the surface of a vacuum-dried (24 h) BaF₂ optical window and sealed inside a vacuum-dried (24 h) Linkam THMS350V temperature-controlled stage. All these operations were performed inside the glovebox and the IR spectra were recorded after removing the stage from the glovebox. The stage was used to protect the sample from decomposition and not for temperature stabilization.

Description of magnetic measurements

Magnetic measurements were performed using Quantum Design MPMS3 Evercool SQUID magnetometer in the magnetic fields up to 7 T for a powdered sample of **ErRe₃** placed under a small quantity of anhydrous benzene in a flame-sealed borosilicate tube. The details of the experimental setup were described by some of us previously (ref. S6). The presence of benzene immobilizes the sample below its freezing point of 278 K. The experimental magnetic data were corrected for the diamagnetism of the sample, benzene and the sample holder. Additional AC magnetic susceptibility data in the 10-10 000 Hz range were recorded using Quantum Design PPMS instrument using the same sample as in the MPMS 3 system.

Details of *ab initio* calculations

To investigate the electronic structure of the compound under study and its magnetic properties, *ab initio* calculations have been carried out with OpenMolcas 19.11 version (ref. S7). The Cholesky decomposition with the threshold of $1.0 \cdot 10^{-7}$ was employed to save disk space. First, a Complete Active Space Self-Consistent Field (CASSCF) calculation (ref. S8) was run by considering eleven electrons spanned by seven 4f-type orbitals. Two different basis sets were considered (Table S5) and both basis sets predict similar energies and values for the *g*-tensors, that give confidence that a much larger, though computationally more expensive basis set, would not change the results significantly. The spin-orbit coupling was introduced within the RASSI module (ref. S9) where all quartet states (35 in total) and all doublet states (112 in total) were admixed by the spin-orbit coupling. Then, magnetic properties were calculated based on the spin-orbital states within the SINGLE_ANISO module (refs. S7, S10 and S11).

The calculated spin-orbit energies (Table S6) demonstrate that the ground Kramers Doublet is well separated from the excited states and shows small transversal components of the *g*-tensor as compared to a very large axial one. This implies that the quantum tunneling of magnetization is suppressed and the relaxation of the magnetization occurs via the excited states. Interestingly, the main magnetic axis is oriented perpendicular to the plane formed by the trigonal Re₃ ligand field (Figure 1C). The relaxation path of the magnetization blocking (Figure 2B) was built as described elsewhere (ref. S12) using SINGLE_ANISO program.

Table S1. Selected crystallographic parameters for **ErRe₃** at 100 and 270 K and the starting material [Cp₂ReH] at 100 K.

Compound	ErRe ₃ (@100 K)	ErRe ₃ (@270 K)	[Cp ₂ ReH]
T / K	100(2)	270(2)	100(1)
CCDC deposition number	2065530	2065531	2027573
Crystal system	trigonal	trigonal	monoclinic
Space group	<i>R</i> -3	<i>R</i> -3	<i>Pn</i>
<i>a</i> / Å	41.1853(10)	41.6196(10)	5.8261(4)
<i>b</i> / Å	41.1853(10)	41.6196(10)	9.9522(6)
<i>c</i> / Å	7.6318(3)	7.6943(3)	13.7335(8)
α / °	90	90	90
β / °	90	90	96.651(2)
γ / °	120	120	90
<i>V</i> /Å ³	11210.9(7)	11542.4(7)	790.94(9)
<i>Z</i>	6	6	4
ρ_{calc} / g cm ⁻³	3.009	2.901	2.657
μ / mm ⁻¹	17.882	17.367	15.284
<i>F</i> (000)	9168	9090	580
Crystal size / mm ³	0.120 x 0.030 x 0.020	0.120 x 0.030 x 0.020	0.210 x 0.170 x 0.060
Instrument	Bruker D8 Quest Eco	Bruker D8 Quest Eco	Bruker D8 Quest Eco
Radiation	Mo K α (λ = 0.71073 Å)	Mo K α (λ = 0.71073 Å)	Mo K α (λ = 0.71073 Å)
2 θ range/°	2.62-33.24	2.59-25.40	2.99-32.72
Reflections collected	46432	112127	2988
Independent reflections	9537	4720	2988
<i>R</i> _{int}	0.0555	0.0845	0.0356
restraints/parameters	6/328	0/310	122/200
<i>R</i> [<i>F</i> _o > 2 σ (<i>F</i> _o)]	0.0543	0.0410	0.0339
<i>wR</i> (<i>F</i> ²)	0.1202	0.0793	0.0892
GOF on <i>F</i> ²	1.082	1.128	1.096
$\Delta\rho_{\text{max}}$, $\Delta\rho_{\text{min}}$ / e·Å ⁻³	4.022, -5.077	1.491, -2.548	2.216, -3.478
Completeness / %	99.5	99.8	99.5

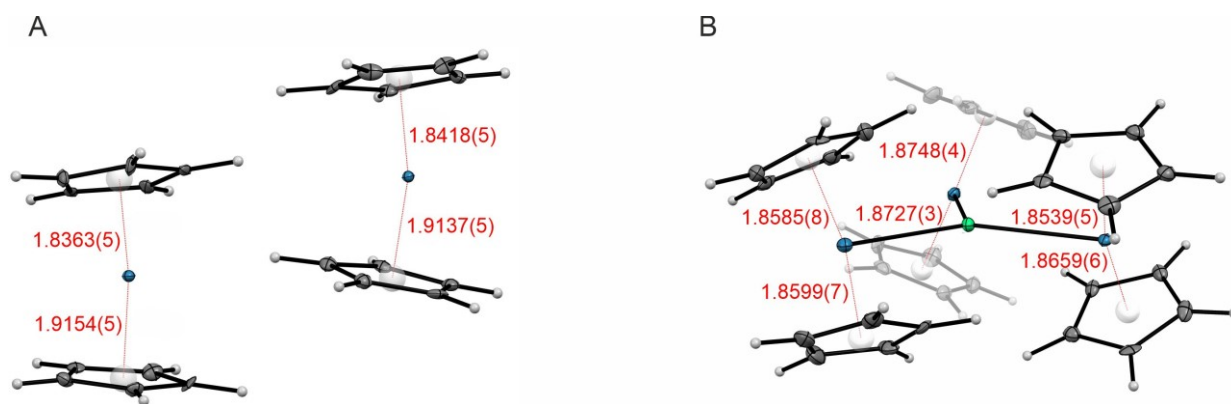


Figure S1. Structural diagrams showing the asymmetric units (ASUs) of the starting material [Cp₂ReH] (A) and the target compound **ErRe₃** (B). The red numbers indicate the distances (Å) between the Re atoms and the centroids of the cyclopentadienyl rings. C – grey, H – light grey, Re – blue, Er – green, centroids – white; ellipsoids at the 40 % probability level for A and 30% for B.

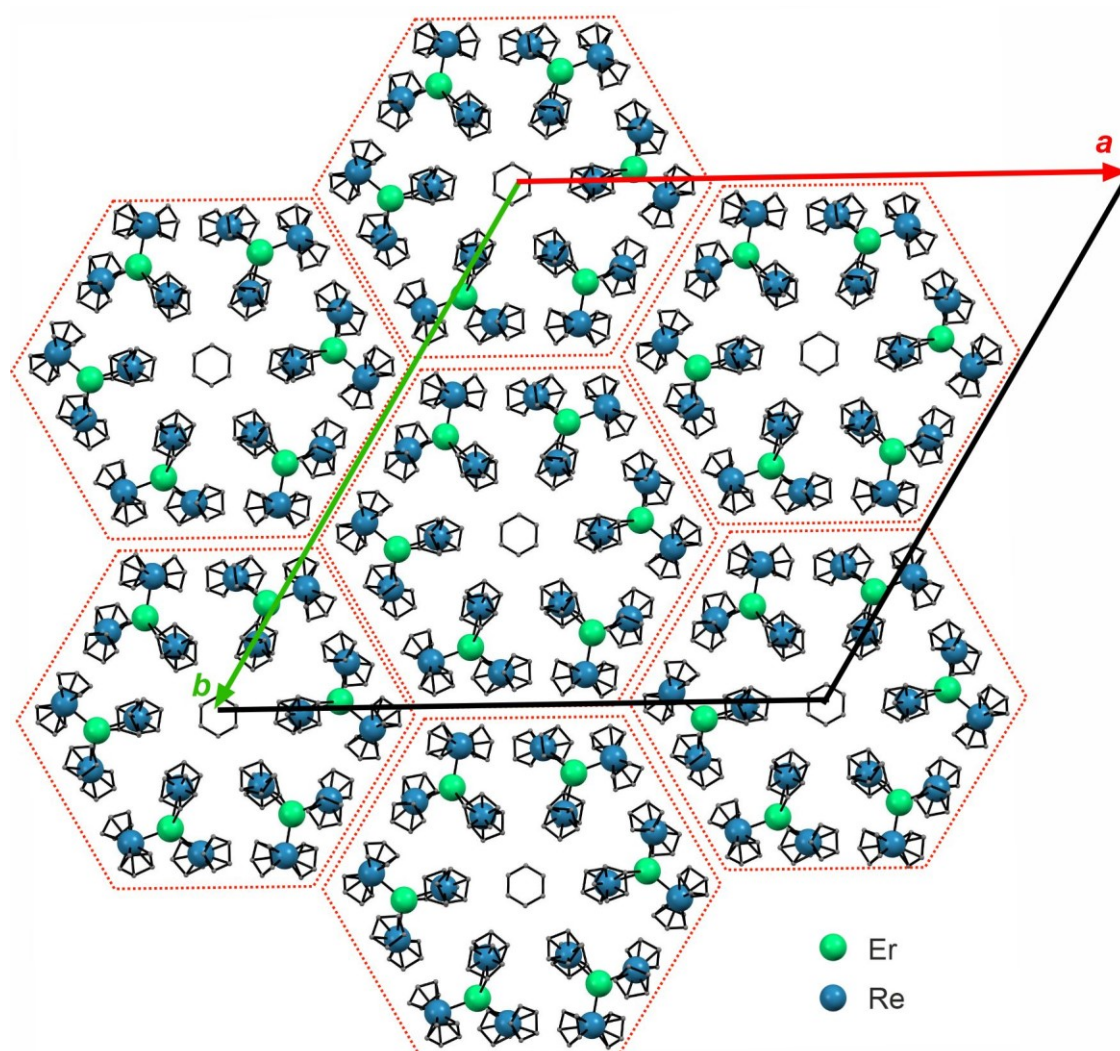


Figure S2. Structural diagram of ErRe_3 as viewed along the c crystallographic direction showing the hexagonal packing pattern of the $[\text{Er}^{\text{III}}(\text{Re}^{\text{I}}\text{Cp}_2)_3]$ molecules highlighted by red dotted hexagons. This type of packing leads to the formation of channels along the c axis filled with benzene molecules (crystallization solvent). Cyclopentadienyl ligands and benzene molecules are represented by black sticks and H-atoms are omitted for clarity.

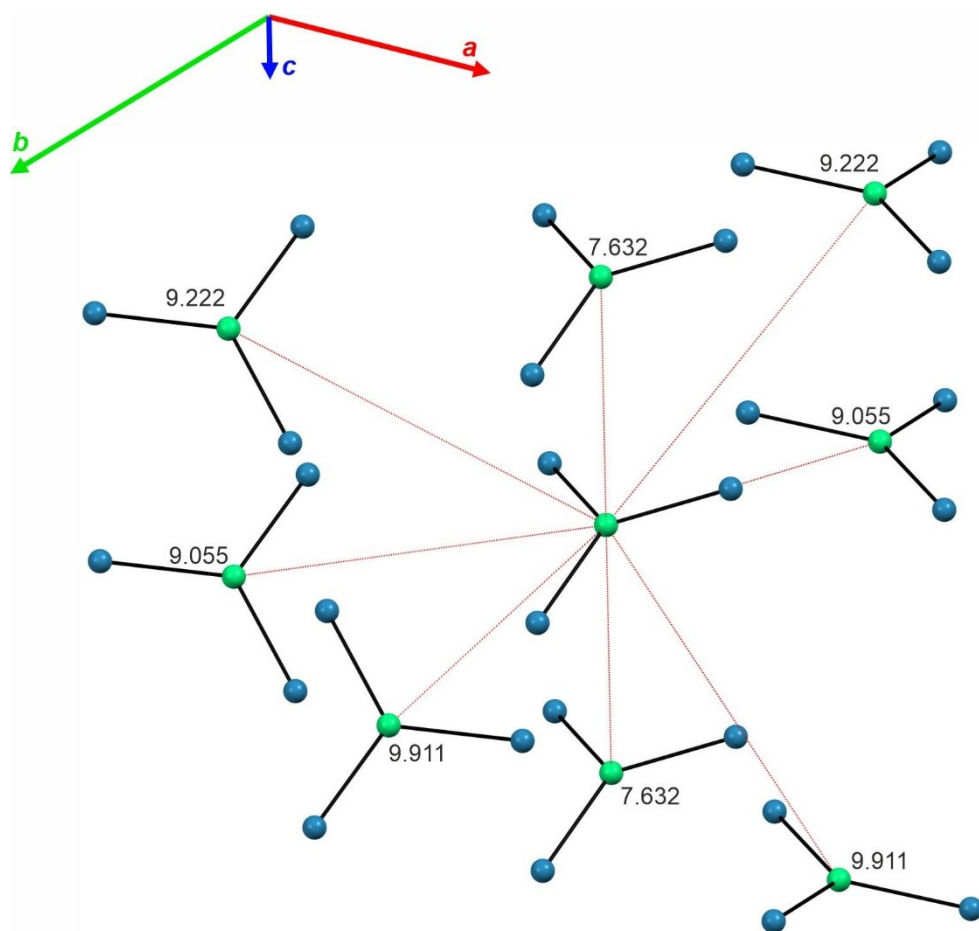


Figure S3. Structural diagram demonstrating and listing Er...Er distances between all ErRe_3 nearest neighbours. The shortest distance is 7.6318(6) Å along the c crystallographic direction.

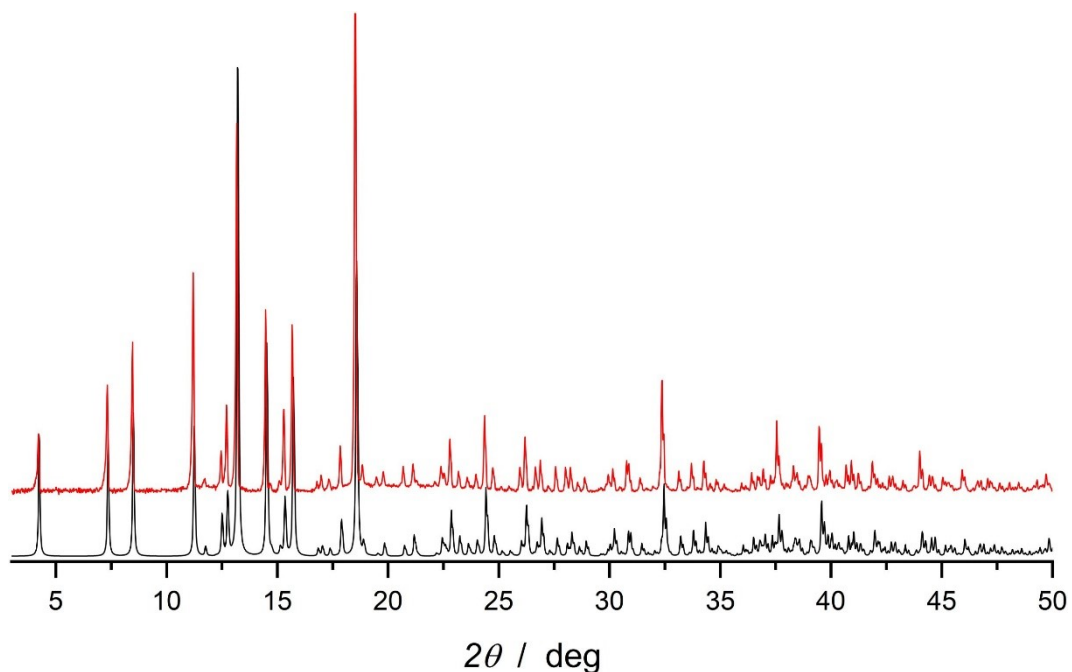


Figure S4. Experimental (red line) and simulated (black line) powder X-ray diffraction experiments for **ErRe₃**. The simulated pattern is calculated based on the 270 K single crystal X-ray diffraction structural model and includes the contribution of the Cu K β which is observed in the experimental pattern.

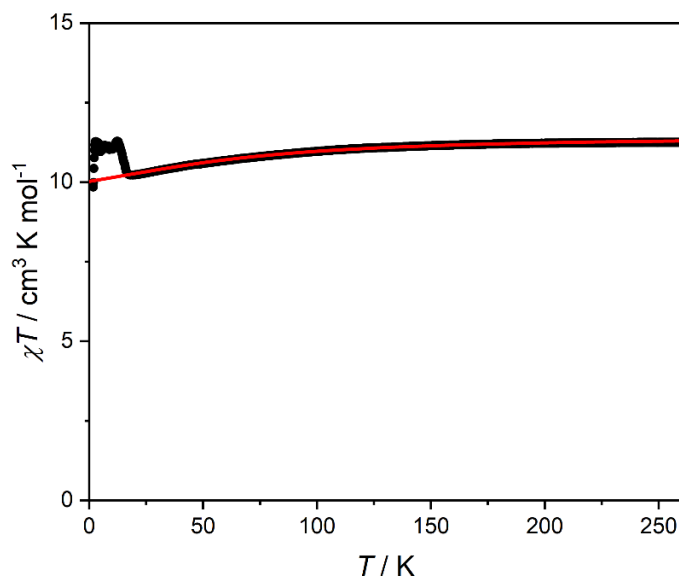


Figure S5. Temperature dependence of the molar magnetic susceptibility and temperature product $\chi T(T)$ for **ErRe₃** recorded at $\mu_0 H = 0.1$ T (black points). The solid red line presents the $\chi T(T)$ obtained from the *ab initio* calculations (see text for details). The observed anomaly below 20 K is caused by the magnetization blocking and the ferromagnetic interactions between the neighbouring ErRe₃ molecules.

Table S2. Results of the generalized Debye model fitting of the frequency dependence of the AC magnetic susceptibility χ' and χ'' for **ErRe₃** recorded at zero magnetic field in the 5.5 – 27 K range presented in Figure 2C (main text).

T / K	χ_s / cm ³ mol ⁻¹	χ_s error	χ_r / cm ³ mol ⁻¹	χ_r error	τ / s	τ error	α	α error	R ²
2.4	1.277	0.050	4.601	0.019	0.00584	1.6E-4	0.206	0.012	0.99963
2.7	1.195	0.049	4.186	0.018	0.00576	1.7E-4	0.202	0.013	0.99958
3.0	1.023	0.044	3.803	0.018	0.00533	1.6E-4	0.218	0.013	0.99946
3.5	0.987	0.036	3.669	0.015	0.00493	1.2E-4	0.208	0.011	0.99961
4.0	0.845	0.046	3.346	0.023	0.00496	1.8E-4	0.240	0.016	0.99904
4.5	0.764	0.039	2.937	0.018	0.00469	1.6E-4	0.234	0.015	0.99917
5.0	0.703	0.032	2.612	0.014	0.00442	1.4E-4	0.225	0.014	0.99932
5.5	0.653	0.029	2.361	0.012	0.00419	1.3E-4	0.217	0.014	0.99937
6.0	0.616	0.026	2.161	0.011	0.00398	1.2E-4	0.206	0.014	0.99941
6.5	0.513	0.019	1.816	0.008	0.00323	8.5E-5	0.191	0.012	0.99947
7.0	0.489	0.017	1.680	0.007	0.00296	7.3E-5	0.172	0.012	0.99954
7.5	0.464	0.015	1.556	0.005	0.00267	6.2E-5	0.153	0.011	0.99962
8.0	0.420	0.013	1.454	0.005	0.00231	5.0E-5	0.146	0.010	0.99958
8.5	0.397	0.011	1.364	0.003	0.00206	4.0E-5	0.130	0.009	0.99970
9.0	0.363	0.010	1.287	0.003	0.00178	3.1E-5	0.124	0.008	0.99970
9.5	0.343	0.009	1.220	0.003	0.00158	2.7E-5	0.114	0.008	0.99975
10.0	0.317	0.007	1.160	0.002	0.00137	2.0E-5	0.108	0.007	0.99977
10.5	0.289	0.009	1.051	0.005	0.0012	2.1E-5	0.083	0.011	0.99936
11.0	0.278	0.010	0.985	0.005	0.00103	2.1E-5	0.059	0.013	0.99900
11.5	0.265	0.009	0.946	0.005	9.13E-4	1.7E-5	0.052	0.012	0.99914
12.0	0.237	0.006	0.913	0.003	7.89E-4	1.0E-5	0.072	0.008	0.99949
12.5	0.218	0.008	0.881	0.004	7.12E-4	1.4E-5	0.081	0.012	0.99879
13.0	0.216	0.007	0.835	0.004	6.14E-4	1.0E-5	0.055	0.011	0.99904
13.5	0.203	0.008	0.815	0.004	5.54E-4	1.1E-5	0.060	0.012	0.99892
14.0	0.205	0.007	0.778	0.003	4.97E-4	8.3E-6	0.031	0.011	0.99919
14.5	0.194	0.007	0.751	0.003	4.43E-4	8.0E-6	0.033	0.011	0.99923
15.0	0.183	0.007	0.729	0.003	3.98E-4	7.4E-6	0.036	0.011	0.99910
15.5	0.170	0.006	0.703	0.003	3.49E-4	6.0E-6	0.038	0.011	0.99894
16.0	0.160	0.004	0.691	0.002	3.16E-4	4.3E-6	0.052	0.008	0.99931
16.5	0.156	0.004	0.666	0.002	2.83E-4	3.2E-6	0.040	0.007	0.99950
17.0	0.151	0.003	0.647	0.002	2.55E-4	2.6E-6	0.038	0.006	0.99962
17.5	0.149	0.003	0.627	0.002	2.31E-4	2.5E-6	0.025	0.007	0.99960
18.0	0.140	0.004	0.608	0.002	2.05E-4	2.8E-6	0.031	0.008	0.99935
18.5	0.138	0.003	0.593	0.001	1.86E-4	1.9E-6	0.023	0.006	0.99966
19.0	0.131	0.002	0.577	0.001	1.64E-4	1.3E-6	0.025	0.005	0.99966
19.5	0.126	0.002	0.565	0.001	1.47E-4	1.2E-6	0.027	0.005	0.99971
20.0	0.121	0.002	0.551	0.001	1.30E-4	8.8E-7	0.028	0.004	0.99974
20.5	0.120	0.002	0.534	0.001	1.16E-4	1.2E-6	0.014	0.007	0.99944
21.0	0.115	0.002	0.525	0.001	1.03E-4	7.4E-7	0.022	0.005	0.99974
21.5	0.114	0.002	0.511	0.001	9.04E-5	8.4E-7	0.013	0.006	0.99961
22.0	0.112	0.004	0.498	0.001	8.0E-5	1.2E-6	0.007	0.009	0.99907
22.5	0.110	0.004	0.488	0.001	7.04E-5	1.0E-6	0.005	0.009	0.99914
23.0	0.106	0.002	0.480	0.001	6.17E-5	4.8E-7	0.011	0.005	0.99978
23.5	0.102	0.005	0.471	0.001	5.41E-5	9.6E-7	0.013	0.011	0.99906
24.0	0.102	0.003	0.460	0.001	4.71E-5	5.6E-7	0.004	0.007	0.99961
24.5	0.100	0.006	0.449	0.001	4.07E-5	8.7E-7	0.000	0.012	0.99898
25.0	0.099	0.006	0.441	0.001	3.54E-5	7.9E-7	0.000	0.012	0.99910
25.5	0.097	0.006	0.435	0.001	3.08E-5	7.2E-7	0.004	0.012	0.99926
26.0	0.096	0.007	0.425	0.001	2.64E-5	7.5E-7	0.000	0.014	0.99917
26.5	0.094	0.008	0.418	0.001	2.27E-5	6.7E-7	0.000	0.013	0.99938
27.0	0.093	0.008	0.411	0.001	1.96E-5	6.0E-7	0.000	0.012	0.99955

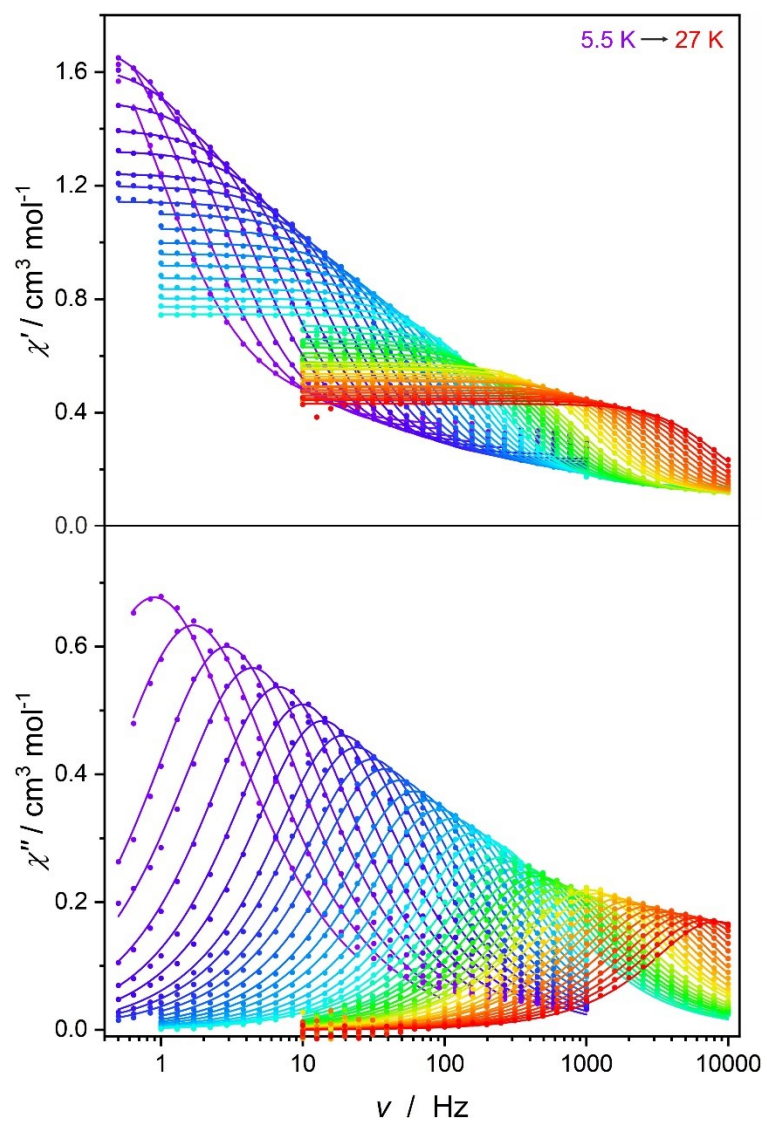


Figure S6. Frequency dependence of the AC magnetic susceptibility χ' and χ'' for **ErRe₃** recorded at $H_{DC} = 0.15$ T in the 5.5 – 27 K range using Quantum Design MPMS3 and PPMS instruments. Solid lines are the best fits to the generalized Debye model. The relevant fitting parameters can be found in Table S3 below.

Table S3. Results of the generalized Debye model fitting of the frequency dependence of the AC magnetic susceptibility χ' and χ'' for **ErRe₃** recorded at $H_{DC} = 0.15$ T in the 5.5 – 27 K range presented in Figure S6.

T / K	$\chi_s / \text{cm}^3 \text{mol}^{-1}$	$\chi_s \text{ error}$	$\chi_r / \text{cm}^3 \text{mol}^{-1}$	$\chi_r \text{ error}$	τ / s	$\tau \text{ error}$	α	$\alpha \text{ error}$	R^2
5.5	0.382	0.004	2.201	0.019	0.1769	0.0033	0.185	0.006	0.99954
6.0	0.348	0.004	1.949	0.013	0.0943	0.0013	0.148	0.006	0.99935
6.5	0.330	0.004	1.749	0.007	0.0549	5.1E-4	0.106	0.005	0.99950
7.0	0.302	0.004	1.644	0.005	0.0362	3.1E-4	0.107	0.005	0.99959
7.5	0.287	0.003	1.507	0.003	0.0235	1.5E-4	0.081	0.004	0.99976
8.0	0.269	0.003	1.403	0.003	0.0160	1.1E-4	0.068	0.004	0.99973
8.5	0.250	0.003	1.325	0.003	0.01151	7.9E-5	0.067	0.004	0.99971
9.0	0.235	0.003	1.244	0.003	0.00831	6.5E-5	0.058	0.005	0.99961
9.5	0.224	0.002	1.200	0.002	0.00663	4.7E-5	0.063	0.004	0.99970
10.0	0.214	0.002	1.145	0.002	0.00517	3.5E-5	0.060	0.004	0.99974
10.5	0.206	0.002	1.103	0.002	0.00423	2.5E-5	0.060	0.004	0.99979
11.0	0.198	0.002	1.050	0.002	0.00331	1.9E-5	0.055	0.004	0.99981
11.5	0.190	0.002	0.999	0.001	0.00261	1.3E-5	0.051	0.003	0.99987
12.0	0.184	0.002	0.959	0.001	0.00214	1.0E-5	0.048	0.003	0.99989
12.5	0.177	0.002	0.918	0.001	0.00174	8.0E-6	0.046	0.003	0.99990
13.0	0.171	0.002	0.874	0.001	0.00140	6.4E-6	0.038	0.003	0.99991
13.5	0.167	0.002	0.834	0.001	0.00116	5.3E-6	0.030	0.003	0.99991
14.0	0.164	0.002	0.802	0.001	9.81E-4	4.4E-6	0.021	0.003	0.99992
14.5	0.161	0.002	0.773	0.001	8.42E-4	3.7E-6	0.014	0.003	0.99993
15.0	0.157	0.002	0.747	0.001	7.25E-4	3.4E-6	0.010	0.003	0.99992
15.5	0.139	0.002	0.708	0.002	6.19E-4	5.5E-6	0.032	0.006	0.99935
16.0	0.136	0.002	0.686	0.002	5.35E-4	5.0E-6	0.027	0.006	0.99929
16.5	0.134	0.002	0.660	0.002	4.59E-4	4.5E-6	0.019	0.006	0.99923
17.0	0.129	0.002	0.646	0.003	4.05E-4	3.6E-6	0.029	0.006	0.99942
17.5	0.125	0.002	0.631	0.003	3.53E-4	3.0E-6	0.031	0.005	0.99949
18.0	0.123	0.002	0.610	0.003	3.06E-4	3.2E-6	0.023	0.007	0.99920
18.5	0.120	0.002	0.595	0.002	2.68E-4	2.7E-6	0.024	0.006	0.99929
19.0	0.117	0.003	0.578	0.002	2.32E-4	3.2E-6	0.020	0.009	0.99877
19.5	0.114	0.002	0.567	0.002	2.03E-4	2.1E-6	0.024	0.007	0.99930
20.0	0.110	0.002	0.553	0.001	1.77E-4	1.7E-6	0.027	0.006	0.99947
20.5	0.114	0.003	0.574	0.002	1.54E-4	1.9E-6	0.031	0.008	0.99914
21.0	0.112	0.003	0.557	0.002	1.31E-4	1.5E-6	0.025	0.007	0.99926
21.5	0.112	0.005	0.537	0.002	1.11E-4	2.2E-6	0.008	0.013	0.99790
22.0	0.108	0.005	0.527	0.002	9.53E-5	1.7E-6	0.012	0.011	0.99845
22.5	0.106	0.004	0.516	0.002	8.21E-5	1.2E-6	0.013	0.009	0.99908
23.0	0.102	0.004	0.511	0.001	7.11E-5	1.0E-6	0.025	0.009	0.99923
23.5	0.102	0.007	0.493	0.002	5.99E-5	1.7E-6	0.008	0.017	0.99729
24.0	0.098	0.004	0.489	0.001	5.17E-5	7.0E-7	0.022	0.008	0.99949
24.5	0.094	0.005	0.480	0.001	4.35E-5	8.1E-7	0.027	0.010	0.99923
25.0	0.094	0.007	0.470	0.002	3.70E-5	9.9E-7	0.022	0.014	0.99875
25.5	0.093	0.008	0.460	0.001	3.16E-5	8.9E-7	0.016	0.014	0.99892
26.0	0.092	0.008	0.451	0.001	2.67E-5	8.0E-7	0.016	0.014	0.99912
26.5	0.089	0.011	0.443	0.001	2.26E-5	8.8E-7	0.017	0.016	0.99899
27.0	0.092	0.017	0.431	0.002	1.95E-5	1.2E-6	0.000	0.025	0.99802

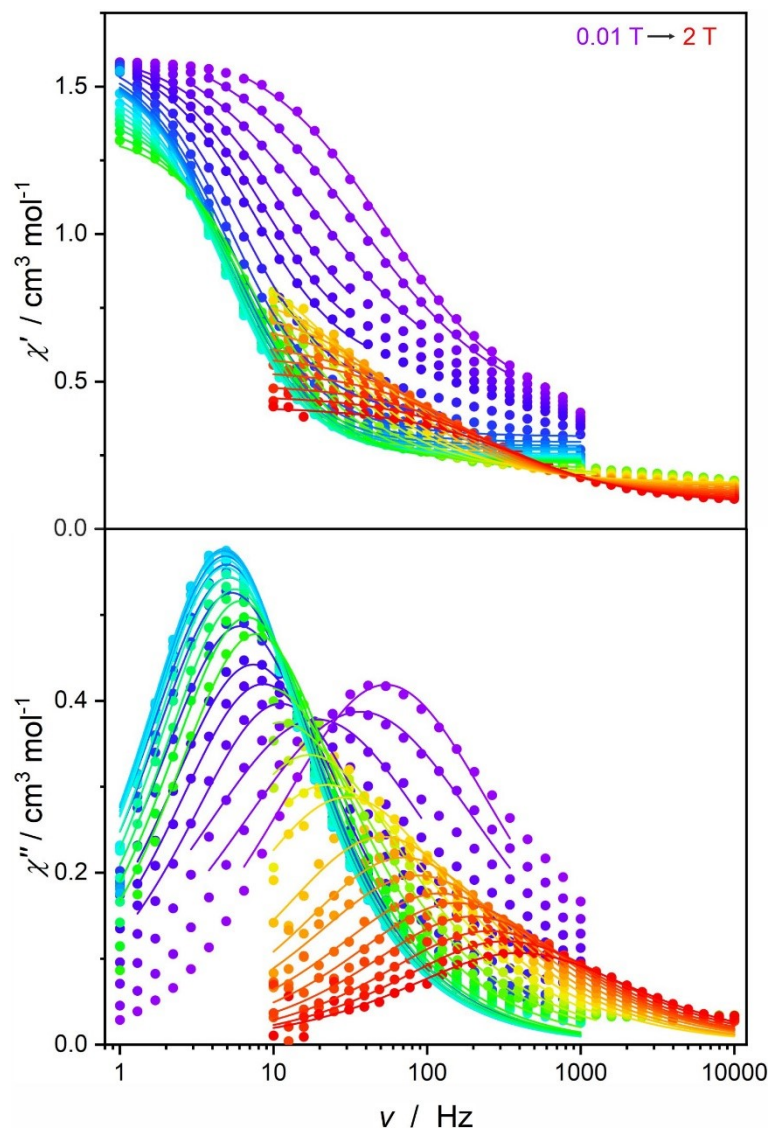


Figure S7. Frequency dependence of the AC magnetic susceptibility χ' and χ'' for **ErRe₃** recorded at $T = 7 \text{ K}$ in the 0.01 – 2 T range using Quantum Design MPMS3 and PPMS instruments. Solid lines are the best fits to the generalized Debye model. The relevant fitting parameters can be found in Table S4 below.

Table S4. Results of the generalized Debye model fitting of the frequency dependence of the AC magnetic susceptibility χ' and χ'' for **ErRe₃** recorded at $T = 7$ K in the 0.01 – 2 T range presented in Figure S6.

H / T	$\chi_s / \text{cm}^3 \text{mol}^{-1}$	$\chi_s \text{ error}$	$\chi_T / \text{cm}^3 \text{mol}^{-1}$	$\chi_T \text{ error}$	τ / s	$\tau \text{ error}$	α	$\alpha \text{ error}$	R^2
0.01	0.371	0.014	1.677	0.013	0.00295	7.1E-5	0.274	0.012	0.99924
0.02	0.352	0.013	1.700	0.013	0.00433	1.1E-4	0.336	0.012	0.99931
0.03	0.442	0.019	1.700	0.017	0.00828	2.6E-4	0.311	0.016	0.99933
0.04	0.583	0.018	1.628	0.010	0.01433	4.1E-4	0.173	0.016	0.99942
0.05	0.559	0.014	1.630	0.010	0.01855	4.1E-4	0.154	0.014	0.99939
0.06	0.517	0.012	1.630	0.012	0.02158	4.3E-4	0.145	0.013	0.99916
0.08	0.442	0.008	1.624	0.011	0.02617	4.2E-4	0.123	0.010	0.99914
0.10	0.374	0.008	1.636	0.013	0.02972	5.6E-4	0.115	0.011	0.99835
0.12	0.313	0.006	1.625	0.017	0.03095	7.5E-4	0.119	0.012	0.99673
0.14	0.294	0.006	1.606	0.016	0.03208	7.1E-4	0.102	0.012	0.99696
0.16	0.281	0.006	1.598	0.016	0.03283	7.0E-4	0.093	0.011	0.99700
0.18	0.273	0.006	1.588	0.017	0.03329	7.3E-4	0.086	0.012	0.99670
0.20	0.266	0.006	1.579	0.017	0.03332	7.4E-4	0.082	0.012	0.99647
0.25	0.254	0.004	1.560	0.011	0.03379	4.9E-4	0.083	0.008	0.99849
0.30	0.247	0.004	1.538	0.010	0.03303	4.4E-4	0.085	0.007	0.99875
0.35	0.243	0.004	1.515	0.010	0.03268	4.3E-4	0.086	0.007	0.99875
0.40	0.239	0.004	1.486	0.010	0.03076	4.6E-4	0.087	0.008	0.99841
0.45	0.235	0.004	1.454	0.011	0.02849	4.5E-4	0.089	0.009	0.99818
0.50	0.231	0.005	1.425	0.011	0.02604	4.4E-4	0.092	0.009	0.99802
0.55	0.227	0.005	1.391	0.011	0.02350	4.2E-4	0.099	0.010	0.99782
0.60	0.222	0.005	1.355	0.011	0.02073	3.9E-4	0.108	0.010	0.99765
0.70	0.205	0.003	1.275	0.032	0.01686	8.6E-4	0.160	0.013	0.99699
0.80	0.188	0.004	1.242	0.029	0.01419	7.2E-4	0.213	0.013	0.99725
0.90	0.183	0.003	1.119	0.016	0.00927	3.0E-4	0.205	0.010	0.99817
1.00	0.170	0.002	1.057	0.010	0.00710	1.5E-4	0.239	0.006	0.99935
1.10	0.154	0.004	1.004	0.018	0.00527	2.4E-4	0.242	0.015	0.99480
1.20	0.149	0.003	0.847	0.008	0.00310	7.8E-5	0.229	0.010	0.99785
1.30	0.142	0.003	0.769	0.007	0.00227	5.3E-5	0.227	0.010	0.99800
1.40	0.132	0.003	0.717	0.005	0.00182	3.9E-5	0.246	0.009	0.99842
1.50	0.124	0.002	0.644	0.004	0.00132	2.6E-5	0.243	0.009	0.99863
1.60	0.119	0.003	0.597	0.005	0.00103	2.6E-5	0.230	0.012	0.99763
1.70	0.113	0.004	0.543	0.005	8.03E-4	2.5E-5	0.228	0.014	0.99670
1.80	0.104	0.004	0.493	0.004	6.29E-4	2.1E-5	0.239	0.015	0.99656
1.90	0.095	0.004	0.454	0.004	4.90E-4	1.7E-5	0.248	0.015	0.99668
2.00	0.085	0.004	0.417	0.003	4.01E-4	1.4E-5	0.272	0.015	0.99704

Table S5. The employed basis sets for *ab initio* calculations.

Basis set 1	Basis set 2
Er.ANO-RCC-VDZP	Er.ANO-RCC-VTZP
Re.ANO-RCC-VDZ	Re.ANO-RCC-VDZP
C.ANO-RCC-VDZ	C.ANO-RCC-VDZP
H.ANO-RCC-VDZ	H.ANO-RCC-VDZ

Table S6. Spin-orbit energies (cm^{-1}) and the *g*-tensors of the lowest in energy Kramers doublets.

Multiplet		Basis set 1	Basis set 2
1		0 0	0 0
2		155.3678 155.3678	154.0022 154.0022
3		252.3421 252.3421	251.7256 251.7256
4		330.1533 330.1533	330.4627 330.4627
5		400.1957 400.1957	400.5357 400.5357
6		482.2936 482.2936	484.0622 484.0622
7		536.0058 536.0058	536.8215 536.8215
8		567.7605 567.7605	568.1037 568.1037
Multiplet			
1	$g_x=$	0.000174	0.000254
	$g_y=$	0.000394	0.000486
	$g_z=$	17.905279	17.905174
2	$g_x=$	0.044452	0.050255
	$g_y=$	0.045268	0.051285
	$g_z=$	15.501484	15.500554
3	$g_x=$	0.027204	0.020446
	$g_y=$	0.095619	0.097873
	$g_z=$	13.092686	13.089441
4	$g_x=$	0.165059	0.176105
	$g_y=$	0.286776	0.296341
	$g_z=$	10.589177	10.573533
5	$g_x=$	4.367102	4.578907
	$g_y=$	4.803154	5.038692
	$g_z=$	7.248873	7.139900

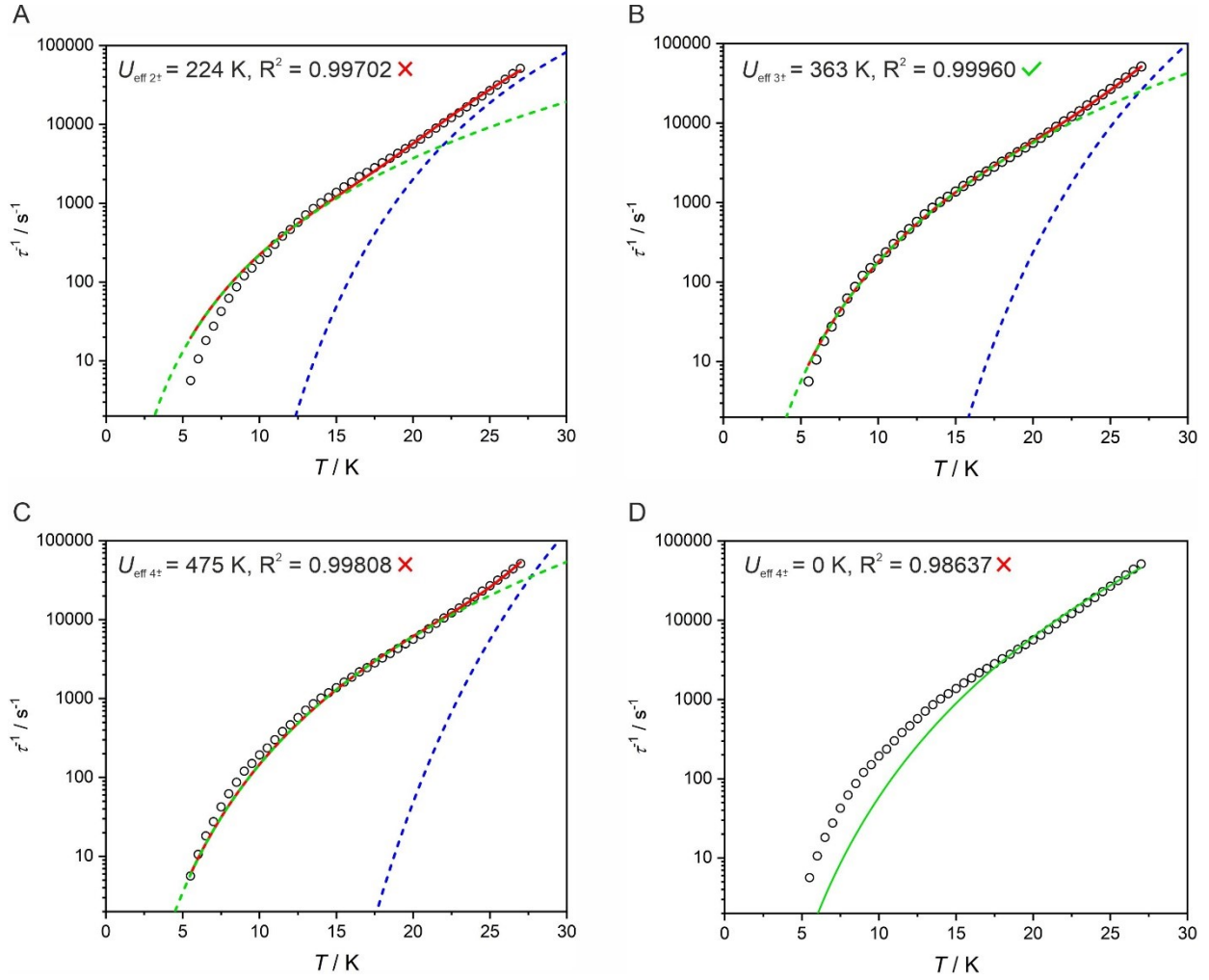


Figure S8. Temperature dependence of the magnetic relaxation rate $\tau^{-1}(T)$ for ErRe_3 under applied 0.15 T DC magnetic field (circles). Solid lines represent the best fits assuming Raman-like and Orbach relaxation processes with C , n , τ_0 as free parameters and U_{eff} fixed at 224 K (A), 363 K (B), 475 K (C) or Raman-like relaxation process only (D). Fitting presented in B shows highest R^2 and is assumed to provide the most accurate value of the energy barrier for magnetization reversal. Fitting assuming Raman-like relaxation only (D) shows the lowest R^2 which sanctions the need for including the Orbach mechanism.

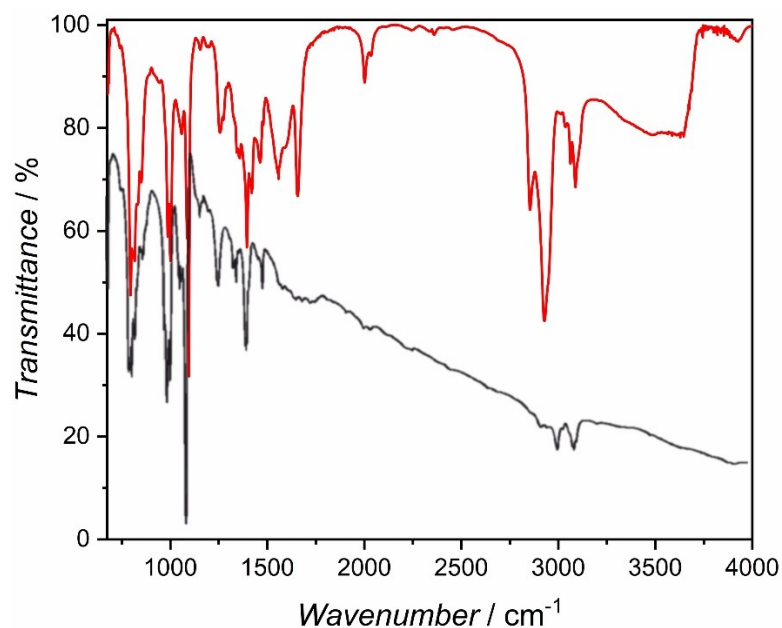


Figure S9. IR spectra of crushed crystals of **ErRe₃** (red solid line) with the overlaid IR spectrum of **SmRe₃** recorded as KBr pellet (black solid line) reproduced from ref. S13 in the 675-4000 cm⁻¹ range (the IR spectrum from Fig. S6 from the Supplementary Information of ref. S13 was traced using CorelDRAW 2019 software). Both spectra are very similar. Weak Re-H stretching modes at 2001 and 2034 cm⁻¹ observed for **ErRe₃** are due to the slight decomposition of this extremely sensitive compound. Note, that these stretches are also present in the IR spectrum of **SmRe₃**, but are largely obstructed by a significant background reaching 40% transmittance at 2000 cm⁻¹ and nearly 15% transmittance at 4000 cm⁻¹.

List of references in the supplemental information

- S1. M. L. H. Green, L. Pratt and G. Wilkinson. 795. Biscyclopentadienylrhodium hydride. *Journal of the Chemical Society (Resumed)*, **1958**, 3916-3922.
- S2. A. G. Avent, C. F. Caro, P. B. Hitchcock, M. F. Lappert, Z. Li and X.-H. Wei. Synthetic and structural experiments on yttrium, cerium and magnesium trimethylsilylmethyls and their reaction products with nitriles; with a note on two cerium β -diketiminates. *Dalton Transactions*, **2004**, DOI: 10.1039/B316695N, 1567-1577.
- S3. H. Zhang, R. Nakanishi, K. Katoh, B. K. Breedlove, Y. Kitagawa and M. Yamashita. Low coordinated mononuclear erbium(III) single-molecule magnets with C_{3v} symmetry: a method for altering single-molecule magnet properties by incorporating hard and soft donors. *Dalton Transactions*, **2018**, 47, 302-305.
- S4. G. M. Sheldrick, *Acta Crystallogr. C*, **2015**, 71, 3–8
- S5. O. V Dolomanov, L. J. Bourhis, R. J. Gildea, J. A. K. Howard and H. Puschmann, *J. Appl. Crystallogr.*, **2009**, 42, 339–341
- S6. M. Ren, D. Pinkowicz, M. Yoon, K. Kim, L.-M. Zheng, B. K. Breedlove, M. Yamashita. Dy(III) Single-Ion Magnet Showing Extreme Sensitivity to (De)hydration. *Inorg. Chem.*, **2013**, 52, 8342-8348.
- S7. F. Aquilante, J. Autschbach, A. Baiardi, S. Battaglia, V. A. Borin, L. F. Chibotaru, I. Conti, L. D. Vico, M. Delcey, I. F. Galván, N. Ferré, L. Freitag, M. Garavelli, X. Gong, S. Knecht, E. D. Larsson, R. Lindh, M. Lundberg, P. Å. Malmqvist, A. Nenov, J. Norell, M. Odelius, M. Olivucci, T. B. Pedersen, L. Pedraza-González, Q. M. Phung, K. Pierloot, M. Reiher, I. Schapiro, J. Segarra-Martí, F. Segatta, L. Seijo, S. Sen, D.-C. Sergentu, C. J. Stein, L. Ungur, M. Vacher, A. Valentini and V. Veryazov. Modern quantum chemistry with [Open]Molcas. *J. Chem. Phys.*, **2020**, 152, 214117.
- S8. B. O. Roos, P. R. Taylor, P. E. M. Sigbahn. A complete active space SCF method (CASSCF) using a density matrix formulated super-CI approach. *Chem. Phys.*, **1980**, 48, 157–173.
- S9. P. Å. Malmqvist, B. O. Roos, B. Schimmelpfennig. The restricted active space (RAS) state interaction approach with spin–orbit coupling. *Chem. Phys. Lett.*, **2002**, 357, 230–240.
- S10. L. F. Chibotaru, L. Ungur. Ab initio calculation of anisotropic magnetic properties of complexes. I. Unique definition of pseudospin Hamiltonians and their derivation. *J. Chem. Phys.*, **2012**, 137, 064112.
- S11. L. Ungur, L. F. Chibotaru. in *Lanthanides and actinides in molecular magnetism* (eds. R. A. Layfield, M. Murugesu) 153–184 (Wiley-VCH Verlag GmbH & Co. KGaA, **2015**).
- S12. L. Ungur, M. Thewissen, J.-P. Costes, W. Wernsdorfer, L. F. Chibotaru. Interplay of strongly anisotropic metal ions in magnetic blocking of complexes. *Inorg. Chem.*, **2013**, 52, 6328–6337.
- S13. M. V. Butovskii, C. Döring, V. Bezugly, F. R. Wagner, Y. Grin and R. Kempe. Molecules containing rare-earth atoms solely bonded by transition metals. *Nature Chemistry*, **2010**, 2, 741-744